Article

Current Biology

Cleavage furrow-directed cortical flows bias PAR polarization pathways to link cell polarity to cell division

Graphical abstract

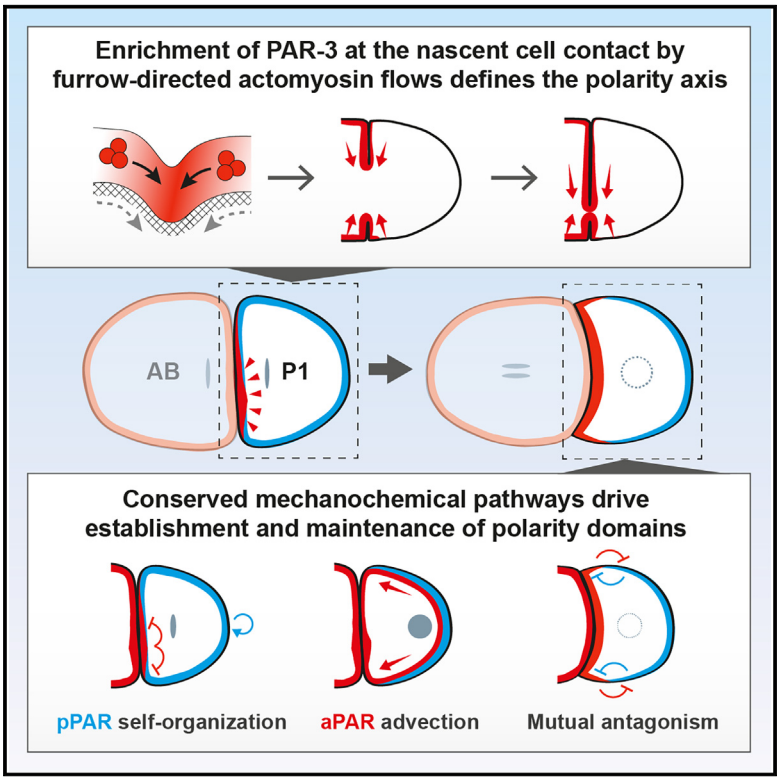

Highlights

- The *C. elegans* P1 blastomere polarizes relative to its new cell contact
- Furrow-directed flow of PAR-3 into the nascent cell contact biases P1 polarity axis
- Similar to the zygote, P1 is polarized by actomyosin flows and PAR network feedback
- Furrow-directed flow induces mirror-symmetric polarity in symmetric daughter cells

Authors

KangBo Ng, Nisha Hirani, Tom Bland, Joana Borrego-Pinto, Susan Wagner, Moritz Kreysing, Nathan W. Goehring

Correspondence

nate.goehring@crick.ac.uk

In brief

Ng et al. show that cleavage furrow-directed actomyosin flows drive accumulation of PAR-3 at the nascent cell contact in dividing *C. elegans* zygotes, which biases the polarization of daughter cells with respect to the division plane.

Ng et al., 2023, Current Biology *33*, 4298–4311
October 23, 2023
https://doi.org/10.1016/j.cub.2023.08.076

CellPress

CellPress
OPEN ACCESS

Current Biology

Article

Cleavage furrow-directed cortical flows bias PAR polarization pathways to link cell polarity to cell division

KangBo Ng,[1,2] Nisha Hirani,[1] Tom Bland,[1,2] Joana Borrego-Pinto,[1] Susan Wagner,[3,4] Moritz Kreysing,[3,4] and Nathan W. Goehring[1,2,5,*]

[1]The Francis Crick Institute, 1 Midland Road, London NW1 1AT, UK
[2]Institute for the Physics of Living Systems, University College London, London WC1E 6BT, UK
[3]Max Planck Institute of Molecular Cell Biology and Genetics, Pfotenhauerstraße 108, 01307 Dresden, Germany
[4]Institute of Biological and Chemical Systems, Karlsruhe Institute of Technology, Hermann-von-Helmholtz-Platz 1, 76344 Eggenstein-Leopoldshafen, Germany
[5]Lead contact
*Correspondence: nate.goehring@crick.ac.uk
https://doi.org/10.1016/j.cub.2023.08.076

SUMMARY

During development, the conserved PAR polarity network is continuously redeployed, requiring that it adapt to changing cellular contexts and environmental cues. In the early *C. elegans* embryo, polarity shifts from being a cell-autonomous process in the zygote to one that must be coordinated between neighbors as the embryo becomes multicellular. Here, we sought to explore how the PAR network adapts to this shift in the highly tractable *C. elegans* germline P lineage. We find that although P lineage blastomeres exhibit a distinct pattern of polarity emergence compared with the zygote, the underlying mechanochemical processes that drive polarity are largely conserved. However, changes in the symmetry-breaking cues of P lineage blastomeres ensure coordination of their polarity axis with neighboring cells. Specifically, we show that furrow-directed cortical flows associated with cytokinesis of the zygote induce symmetry breaking in the germline blastomere P1 by transporting PAR-3 into the nascent cell contact. This pool of PAR-3 then biases downstream PAR polarization pathways to establish the polarity axis of P1 with respect to the position of its anterior sister, AB. Thus, our data suggest that cytokinesis itself induces symmetry breaking through the advection of polarity proteins by furrow-directed flows. By directly linking cell polarity to cell division, furrow-directed cortical flows could be a general mechanism to ensure proper organization of cell polarity within actively dividing systems.

INTRODUCTION

The conserved PAR (*par*-titioning defective) polarity network underlies cell polarity in a variety of developmental processes, including cell motility, asymmetric cell division, and tissue patterning. As the network is redeployed across diverse cell and tissue types, it must continuously adapt to changing cellular contexts and environmental cues. To understand how the PAR network adapts during development, we turned to the *C. elegans* germline P lineage as a model.

The germline precursors in *C. elegans* are set aside during a program of four sequential PAR-dependent asymmetric stem cell-like divisions.[1,2] Beginning with the zygote (P0) and proceeding through P1, P2, and P3, each cell polarizes and undergoes an asymmetric division to yield a P lineage daughter and a somatic sister (Figure 1A). These asymmetric divisions ultimately give rise to the germline founder cell, P4, which divides symmetrically to generate the two primordial germ cells, Z2 and Z3.[1,2]

In the zygote, PAR polarity relies on mutual antagonistic feedback between two groups of proteins that form opposing membrane-associated domains (Figure 1A): anterior PAR (aPAR) proteins (PAR-3, PAR-6, atypical protein kinase C [aPKC/PKC-3], and CDC-42) and posterior PAR (pPAR) proteins (PAR-1, PAR-2, LGL-1, and CHIN-1).[3–11] Each group excludes the other from its respective membrane domain: the polarity kinase PKC-3 excludes pPARs from the anterior, whereas the kinase PAR-1 and the CDC-42 GAP CHIN-1 exclude aPARs from the posterior.[9,12,13]

Prior to symmetry breaking, aPARs are enriched uniformly throughout the plasma membrane and restrict pPARs to the cytoplasm.[14,15] Symmetry is broken through two semi-redundant cell-intrinsic cues (Figure 1A). First, cortical actin flows segregate aPARs toward the anterior half of the cell, which allows loading of pPARs onto the posterior membrane.[16,17] Second, pPAR domain formation is promoted by the self-organization of PAR-2.[12,18,19] This so-called PAR-2 pathway relies on the combined effects of the RING domain and microtubule-binding activity of PAR-2, which provide for membrane stabilization and local protection from PKC-3 phosphorylation at the posterior, respectively.[12,19] As the pPAR domain forms, PAR-2

CellPress
OPEN ACCESS

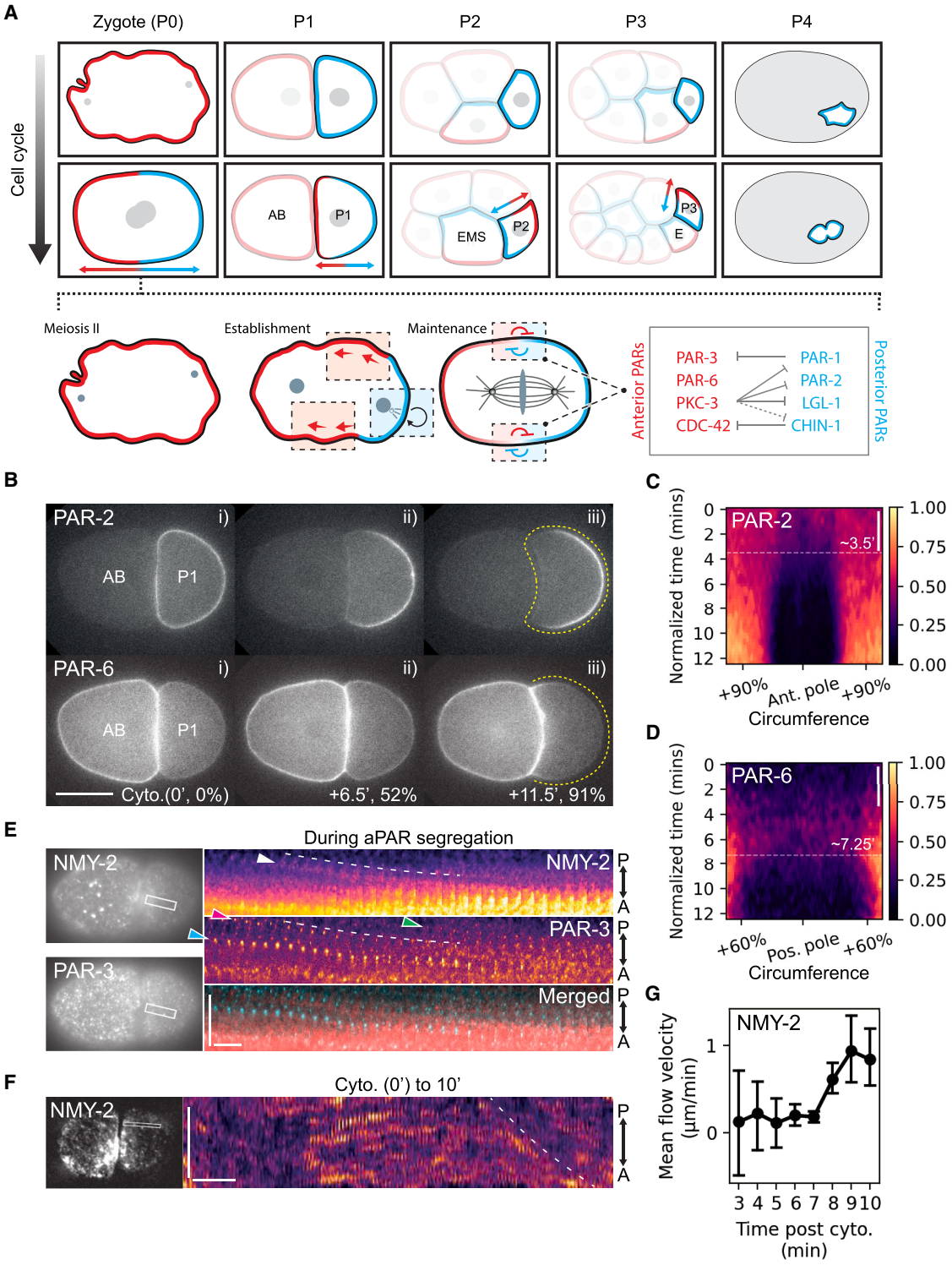

Figure 1. PAR polarization during P1 polarity establishment

(A) (Top) A schematic of PAR protein localization in each blastomere at early and late stages of the cell cycle. Note that PAR domains in P1, P2, and P3 are oriented with respect to their neighbors AB, EMS, and E, respectively. (Below) Mechanisms of polarization as understood from work in the zygote. In the zygote, aPARs (red) are initially uniformly enriched on the membrane, whereas pPARs (cyan) are cytoplasmic. The centrosome then induces symmetry breaking by triggering cortical flows (dashed red box), and induces self-organization of a PAR-2 domain (dashed blue box) at the posterior. Segregation of aPARs and pPARs is then maintained via mutual antagonism (dashed box with gradient).

(legend continued on next page)

stabilizes PAR-1, which in turn promotes local displacement of aPARs through phosphorylation of PAR-3.[12]

Previous work has shown that asymmetric divisions of P1–P3 are associated with asymmetric PAR protein localization[1] and retain a dependence on PKC-3 for polarization,[20] consistent with a continued requirement of PAR polarity. The anterior-directed flow of myosin and PAR-6 has also been observed in P1.[17,21] However, there are key differences in the pattern of polarization between the zygote and later P blastomeres. For example, P1–P3 are all born with a cortex enriched for pPARs, a configuration that is inverted relative to the zygote[20,22] (Figure 1A). Importantly, and in contrast to the zygote, polarity in P1–P3 must be oriented with respect to its neighbors to ensure proper positioning of cells within the embryo (Figure 1A). Thus, comparative analysis of polarization of the zygote relative to later P lineage blastomeres provides an ideal context for understanding how an initially cell-autonomous polarity network adapts to the onset of multicellularity to allow for coupling of polarity between neighbors.

Here, we show that cleavage furrow-directed cortical flows break symmetry in P1 by concentrating a persistent pool of aPARs at the nascent cell contact, which then biases the polarity axis of P1. In doing so, PAR domains in P1 become aligned and coordinated with respect to the position of its sister cell, AB. As furrow-directed flows provide a simple physical mechanism for enriching signaling molecules at cell contacts, they likely play a widespread role in organizing cell polarity in actively dividing systems.

RESULTS

P1 blastomeres rely on the same mechanochemical pathways as the zygote for PAR polarization

As the emergence of PAR polarity in P1 is largely unexplored, we first sought to characterize the behavior of aPARs and pPARs through the cell cycle (Figures 1A and 1B). We found that pPARs were initially uniformly enriched throughout the membrane, whereas aPARs were mostly confined to the cytoplasm, a configuration that is inverted with respect to the zygote (Figures 1B–1Bi and S1). The first observable sign of polarization in P1 occurred within 3–5 min following the completion of cytokinesis of the zygote, when PAR-2 concentrates to form a posterior domain and clears from the nascent cell contact (Figures 1B–1Bii, 1C, S1A, and S1B). We were unable to exclude preferential enrichment of aPARs at the P1 cell contact at this stage, due to confounding aPAR signals coming from AB. However, away from the contact, we observed aPAR loading throughout the membrane, such that aPARs and pPARs overlapped in the posterior (Figures 1B–1Bii and S1C–S1F). Only after ~7 min, did aPARs begin to segregate away from the posterior (Figures 1B–1Biii and 1D). Finally, by ~10 min, P1 exhibited the typical, mutually exclusive arrangement of aPARs and pPARs (Figures 1B–1Biii; Video S1). Interestingly, despite ostensible differences in the pattern of polarity emergence between the zygote and P1, aPAR exclusion from the posterior in P1 also occurred coincidentally with flows of NMY-2, which moved together with PAR-3 toward the anterior (Figures 1E–1G).

Next, we examined the mechanisms that underlie the establishment of polarity in P1. In the zygote, aPAR segregation depends semi-redundantly on cortical actin flows and exclusion from the posterior by PAR-1[12] (Figure 1A). We therefore disrupted cortical flows and pPAR antagonism alone or in combination in P1 (Figure S2) by taking advantage of (1) a fast-acting *nmy-2(ts)* allele to selectively block flows only after completion of cytokinesis of the zygote[23] and (2) the *par-3(S950A)* allele that prevents the phosphorylation of PAR-3 by PAR-1[12]. Because of the redundant nature of cortical flows and pPAR exclusion, asymmetric division of the zygote was normal in *par-3(S950A)* embryos so long as flows were present (Figures S3).

We observed only minor effects on aPAR segregation in P1 in *par-3(S950A)* embryos or *nmy-2(ts)* embryos in which we acutely disrupted flows (Figures 2A and S2). However, when both pathways were inhibited, i.e., *nmy-2(ts); par-3(S950A)* embryos, aPARs no longer cleared from the posterior pole efficiently (Figures 2A and S2A). Note that the formation of a PAR-2 domain was largely normal in all conditions, consistent with the fact that PAR-2 domain formation precedes segregation of aPARs away from the posterior (Figure S2B). Thus, similar to the zygote, both cortical flows and pPAR antagonism play semi-redundant roles in driving aPAR segregation away from the posterior in P1.

We then shifted our focus to understanding the mechanisms that drive pPAR polarization in P1. In the zygote, formation of a posterior pPAR domain is achieved via anterior exclusion by PKC-3 and the PAR-2 pathway, the latter of which depends on microtubule-binding activity and the RING domain of PAR-2.[12,19] Surprisingly, in P1, the PAR-2 microtubule-binding mutant, PAR-2(MT−), polarized even earlier than PAR-2(WT) (Figures 2B and 2F; zygote localization in Figure S4A). Moreover, polarization of PAR-2 in P1 was also unaffected by microtubule depolymerization (Figure S4G), suggesting that early PAR-2 polarization in P1 does not depend on its microtubule-binding ability. By contrast, the RING-disrupting mutant, PAR-2(C56S), polarized late and only showed loading onto the posterior membrane at a time that coincided with the onset of aPAR

(B) Midsection confocal images of embryos expressing mCherry::PAR-2 and PAR-6::mNG (NWG0268) at indicated times. Yellow dashed lines indicate the region used for membrane quantification in (C) and (D). Scale bars, 20 μm. Time is indicated in minutes and % interval between cytokinesis and nuclear envelope breakdown (NEBD). See also Video S1.

(C and D) Averaged spatiotemporal profile of PAR-2 and PAR-6 membrane levels (n = 6). Scale bars, 3 min. Time of individual videos was normalized to the interval between cytokinesis and NEBD (12.6 ± 0.34 min). Dashed lines indicate the mean time of PAR segregation.

(E) Cortical images and kymograph of PAR-3::GFP and NMY-2::mKate (NWG0150) during aPAR segregation (n = 6) in P1. White box indicates the region of the kymograph. (Top) White arrowhead indicates myosin movement toward the anterior. (Bottom) Green, magenta, and cyan arrowheads indicate PAR-3 movement toward the anterior. Scale bars, horizontal, 10 s; vertical, 10 μm.

(F) Representative cortical images and kymograph of NMY-2::GFP (LP162). Scale bars, horizontal, 1 min; vertical, 10 μm. Dashed line indicates onset of flows.

(G) Quantification of particle image velocimetry (PIV) analysis of NMY-2 flow velocity at indicated times (n = 5). Mean and 95% confidence intervals (bootstrapped) are shown.

See also Figure S1.

CellPress
OPEN ACCESS

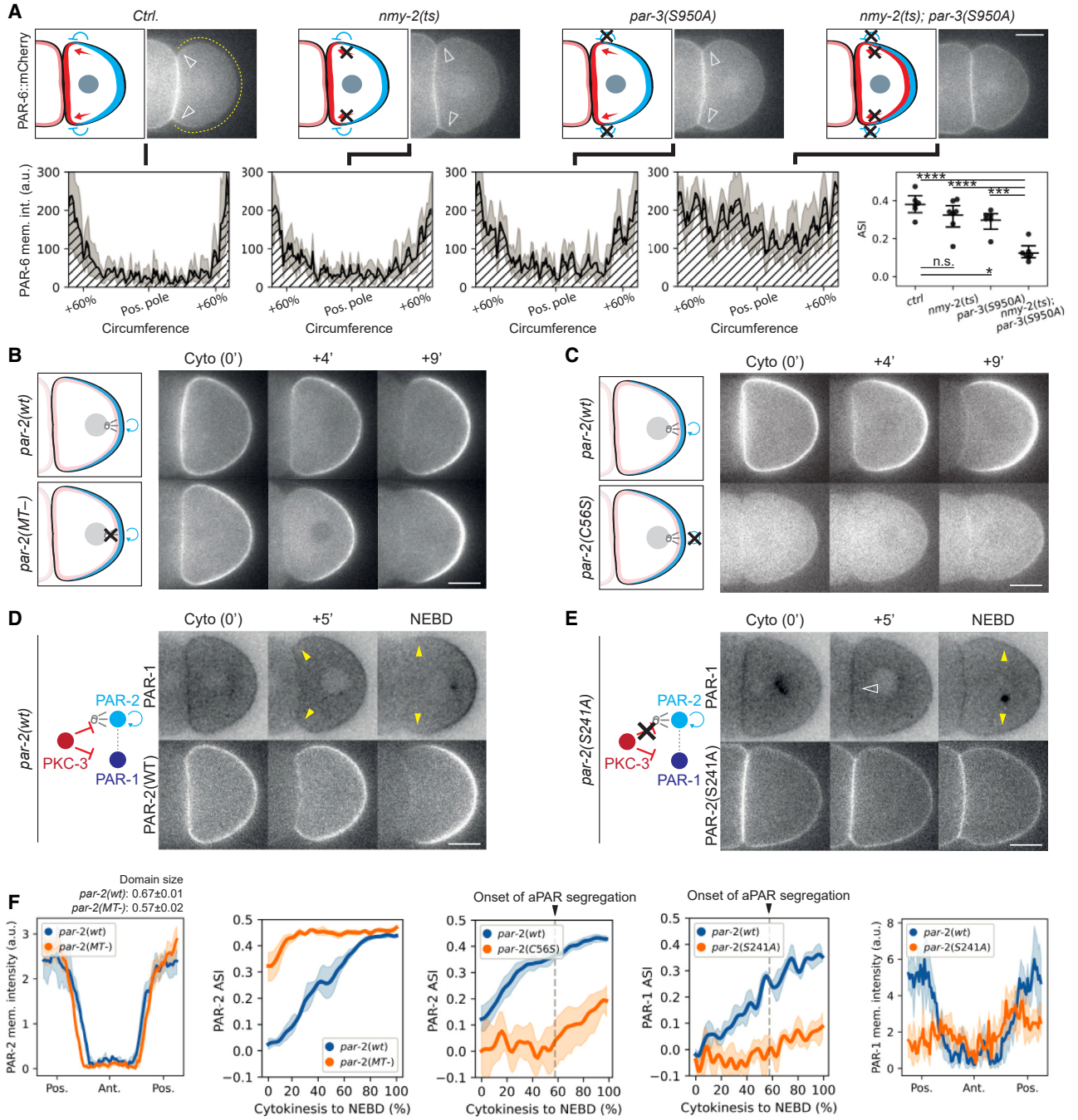

Figure 2. PAR polarization in P1 utilizes conserved mechanochemical pathways

(A) (Top) Midsection confocal images of embryos expressing PAR-6::mCherry in a wild type (Ctrl; NWG0076) (n = 6), *nmy-2(ts)* (NWG0283) (n = 7), *par-3(S950A)* (NWG0258) (n = 6), or a double *nmy-2(ts)*; *par-3(S950A)* background (NWG0319) (n = 7) at NEBD. Red arrows, flows; blue inhibitory arrow, aPAR exclusion by pPARs. Open arrowheads indicate PAR-6 segregation toward the anterior. (Bottom) Quantification of PAR-6 membrane distribution extracted from around the non-contact membrane as indicated in the control embryo (dashed yellow line), with a comparison of measured asymmetry (ASI, asymmetry index). Student's t test was performed, unpaired, two-tailed. Mean and 95% confidence interval (bootstrapped) indicated. See also Figure S2B.

(B–E) A time series of midsection confocal images of embryos expressing GFP::PAR-2 (KK1273) (n = 4) or GFP::PAR-2(MT–) (NWG0192) (n = 5) (B); mNG::PAR-2 (LP637) (n = 6) or mNG::PAR-2(C56S) (NWG0240) (n = 8) (C); PAR-1::GFP with either mCherry::PAR-2 (NWG0332) (n = 4) (D); or mCherry::PAR-2(S241A) (NWG0344) (n = 5) (E). Open arrowhead highlights slower clearance of PAR-1 from the anterior (cell contact) of *par-2(S241A)* embryos. Closed yellow arrowheads roughly indicate the extent of the PAR-1 domain.

(legend continued on next page)

segregation (Figures 1D, 2C, and 2F; zygote localization in Figure S4B). This phenotype is unlikely to be solely due to defects in asymmetric division of the zygote, as PAR-2 still polarizes early when fate specification is disrupted by depleting MEX-5[21] (Figures S4E and S4F; see also mirror-symmetric polarization of 2-cell embryos, Figure 6). Thus, as in the zygote, the RING domain is required to support PAR-2 domain formation on aPAR-enriched membranes.[19] Importantly, suppression of PAR-2 polarization[12] led to weaker and delayed polarization of PAR-1 (Figures 2D–2F, S4C, and S4D) such that it occurred concurrently with, instead of prior to, the onset of aPAR segregation (Figure S4H), consistent with a requirement for the PAR-2 pathway for robust and timely pPAR polarity in P1.

Altogether, these data indicate that despite variations in how polarity emerges in P1 (compare Figure 1A to Figure 1B), the mechanochemical pathways driving aPAR and pPAR domain formation that operate in the zygote also operate in P1. A key difference, however, is that PAR-2 polarization in P1 appears to have lost its dependence on the microtubule cue, suggesting that the symmetry-breaking cues may differ.

Furrow-directed flows enrich PAR-3 within the nascent cell contact

Given that P1 cells use similar mechanochemical pathways for PAR polarization as the zygote, we next wondered how the pathways were spatially biased such that the polarity axis of P1 was consistently oriented with respect to AB (Figure 1A). The first sign of this bias was the invariable segregation of pPARs away from the nascent cell contact (Figures 1B, 1C, 2B–2F, and S2B), which did not rely on the microtubule-binding activity of PAR-2. This suggested the presence of an early-acting symmetry-breaking cue that biases the orientation of P1 polarity shortly after its birth.

While imaging aPARs at the cortex of P1 cells, we noticed that PAR-3 was transported into the nascent cleavage furrow by furrow-directed cortical flows as the zygote divided (Figures 3A–3D; Video S2). This was particularly prominent in *par-3(S950A)* embryos, which exhibited elevated levels of PAR-3 at the membrane (Figure 3B). Notably, directed movement of PAR-3 toward the midcell was lost when we disrupted the actomyosin cortex acutely before cytokinesis (Figures 3C and 3D), indicating that directional PAR-3 transport was actomyosin dependent. Subsequent imaging of dividing embryos in cross-section revealed an enrichment of PAR-3 toward the leading edge of the ingressing furrow, similar to what was reported by Pittman and Skop[24] (Figures 3E–3G). Importantly, we found that this was not observed for the plasma membrane marker PH-PLCd1 and thus does not simply reflect an increased membrane accumulation at this site. Together, these data suggest that PAR-3 specifically flows toward the leading edge of the cleavage furrow during cytokinesis.

Note that these furrow-directed flows occur during division of the zygote and are distinct from the flows that we documented above in Figures 1F and 2A, which occur ~7 min after completion of division of the zygote (“late” flows). Importantly, these “early” furrow-directed flows would have been intact in the *nmy-2(ts)* experiments shown in Figures 2A and S2 in which we shifted the temperature only after cytokinesis was complete, and thus furrow-dependent localization of PAR-3 at the cell contact would have been normal.

We next sought to follow the fate of PAR-3 accumulation in the furrow after the zygote divided. However, visualization of aPARs specifically at the nascent cell contact in P1 is complicated by the coincidence of fluorescence signals coming from both AB and P1, especially because AB inherits higher levels of aPARs relative to P1. To specifically visualize proteins in P1, we devised a photobleaching technique to remove the contribution of fluorescence signals from AB (Figures 4A and S5). Briefly, just after cytokinesis, we bleached the entire AB cell, which necessarily includes a portion of the P1 membrane at the contact site. This was followed by continuous bleaching of a region of AB away from the cell contact to bleach any residual pool of fluorescent protein in AB. After a brief period (1–2 min) to allow fluorescence recovery within P1, we could then assess the distribution of protein specifically on the P1 side of the AB-P1 contact.

Applying this approach to PH-PLCd1 revealed a uniform enrichment throughout the plasma membrane of P1 (Figures 4A and S5; Video S3). By contrast, we found a persistent pool of PAR-3 localized to the contact site (Figures 4B and S5; Video S3). Both visual inspection and quantification of spatial intensity profiles along the contact site revealed a biased accumulation of PAR-3 toward the site of furrow closure (Figures 4A, 4B, 4D, and S5). Taken together, our data suggest that furrow-directed flows transport PAR-3 toward the leading edge of the ingressing furrow, thereby establishing a pool of PAR-3 at the contact site (anterior) of the newly born P1 cell.

To confirm that furrow-directed transport was sufficient to account for the enrichment of PAR-3 at the nascent cell contact, we asked whether we could induce enrichment of another molecule at the contact site by modifying it to “sense” flows. Prior work showed that the posterior protein PAR-2 could be re-engineered to sense cortical flows by introducing an oligomerization domain and mutating a key PKC-3 phosphosite.[25] This protein, PAR-2(S241A; 4mer), unlike PAR-2(WT), was efficiently segregated by cortical flows toward the anterior of the zygote along with aPARs[25] (Figure 4C). Consistent with the idea that furrow flows can enrich molecules at the cell contact, PAR-2(S241A; 4mer) exhibited a near identical pattern of accumulation at the nascent cell contact as PAR-3 (Figures 4D and S5).

In the zygote, PAR-3 biases the loading of PAR-6/PKC-3 onto the plasma membrane, directing their enrichment within the anterior PAR domain.[26] Consistent with events in the zygote, we found that PAR-6 was also enriched at the cell contact (anterior) of P1 (Figure 4E). This suggests a model in which furrow-directed flows establish a stable pool of aPARs at the cell contact, which is thereby positioned to bias polarization of pPARs and thus define the polarity axis of P1 relative to the position of AB.

(F) Quantification of either ASI over time or membrane distributions for conditions corresponding to (B)–(E). Dashed lines indicate approximated onset of aPAR segregation as shown in Figure 1. Mean and 95% confidence interval (bootstrapped) indicated.
Scale bars, 10 μm. n.s., not significant, * p value < 0.05, ** p value < 0.005, *** p value < 0.0005, **** p value < 0.00005.
See also Figures S2–S4.

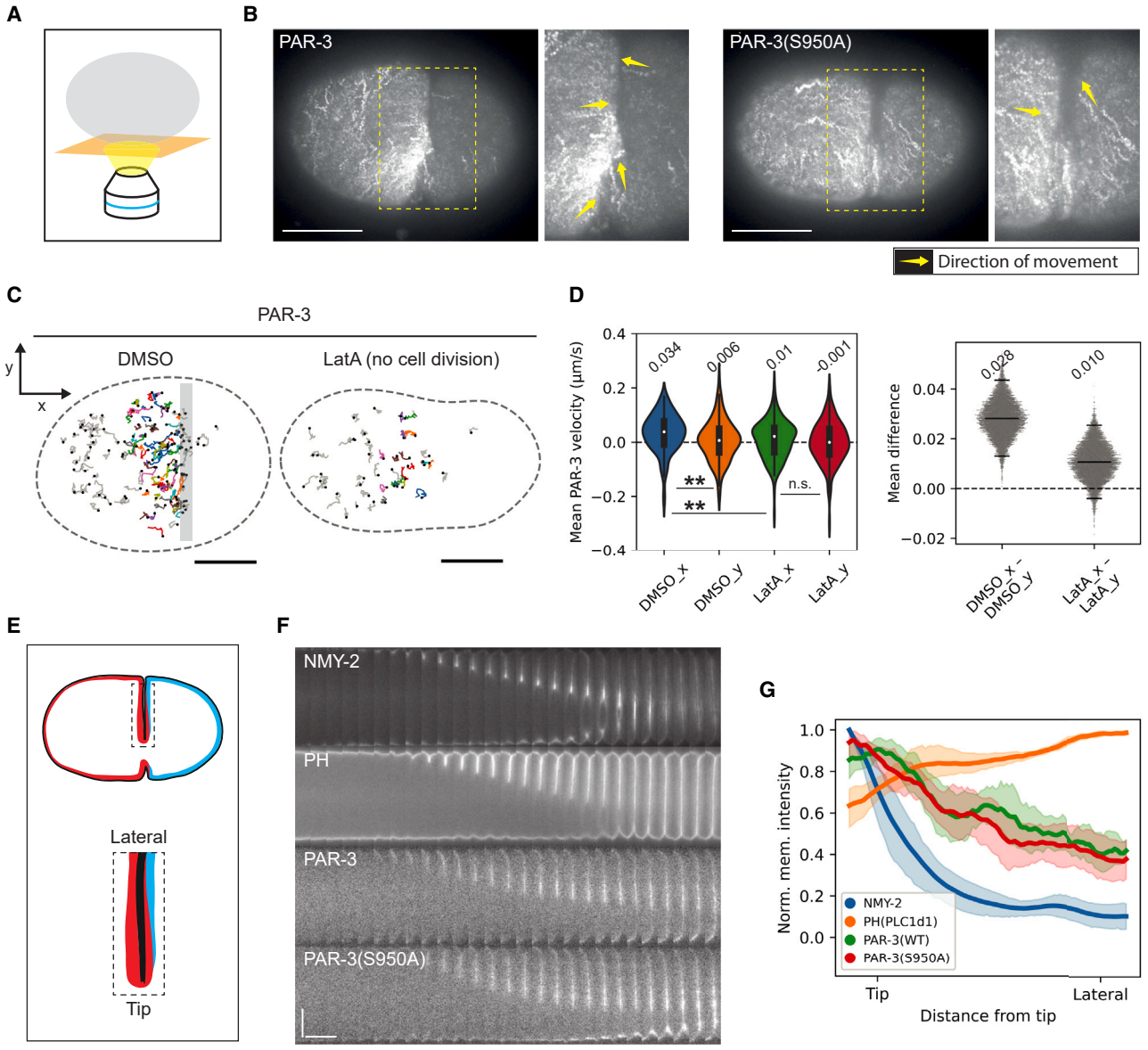

Figure 3. Midzone-directed cortical flows drive PAR-3 enrichment into the nascent cleavage furrow

(A) A schematic illustrating the optical section during cortical imaging.

(B) Time-averaged cortical images of mNG::PAR-3 (NWG0189) (n = 5) and mNG::PAR-3(S950A) (NWG0259) (n = 5) spanning 182.5 s during furrow closure, which reveals directed tracks of cortical clusters toward the ingression site (yellow arrows). Scale bars, 20 μm. See also Video S2.

(C) Tracks of PAR-3 movement 200–500 s after anaphase in either DMSO or latrunculin A (0.5 μM) treated embryos. As latrunculin-treated embryos do not form a cleavage furrow, we analyzed tracks within a comparable region defined as the 35%–65% of embryo length, which is a region just the anterior of the furrow position, in DMSO-treated embryos (furrow position = gray bar). Scale bars, 20 μm.

(D) (Left) Violin plot of mean PAR-3 velocity for a region corresponding to the colored tracks shown in (C). DMSO: 174 tracks, 3 embryos. LatA: 176 tracks, 5 embryos. Student's t test, unpaired, two-tailed. (Right) Bootstrapped mean difference comparing (1) DMSO_x and DMSO_y and (2) LatA_x and LatA_y. Lines indicate mean and 95% percentile. Mean is indicated above each condition in both plots. Scale bars, 20 μm.

(E) A schematic illustrating the region of interest (ROI) and nomenclature used when observing leading edge enrichment of molecules during furrow closure.

(F) Kymograph of embryos expressing NMY-2::GFP (LP162) (n = 5), GFP::PH(PLC1d1) (OD58) (n = 5), mNG::PAR-3 (NWG0189) (n = 7) and mNG::PAR-3(S950A) (NWG0259) (n = 6) during furrow closure. Scale bars, vertical, 10 μm; horizontal, 20 s.

(G) Distribution of indicated proteins at the ingressing furrow 30 s before cytokinesis completion. Fluorescence is normalized by intensity and distance from the tip to lateral edge. Mean and 95% confidence interval (bootstrapped) indicated.

n.s., not significant, * p value < 0.05, ** p value < 0.005, *** p value < 0.0005, **** p value <0.00005.

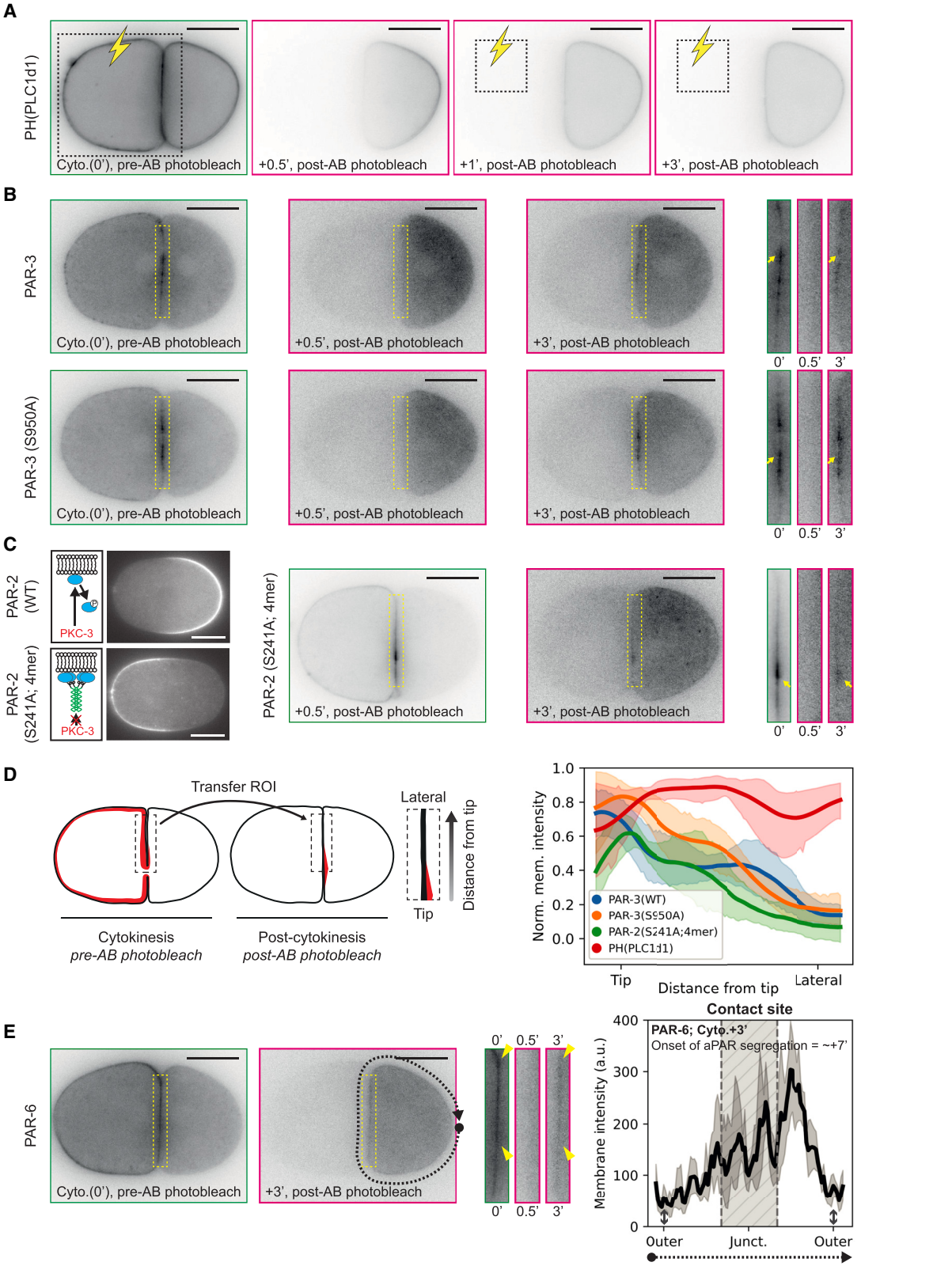

(legend on next page)

Enrichment of aPARs at the nascent cell contact biases the PAR polarity axis in P1

We next sought to confirm a functional role for this furrow-associated enrichment of aPARs at the contact in orienting the axis of pPAR polarization in P1. To validate the role of aPAR activity in clearing pPARs from the contact site, we utilized an analog-sensitive version of PKC-3, PKC-3AS, which allowed acute inhibition of aPAR activity in P1 using the ATP analog 1NA-PP1.[27] Consistent with a requirement for aPAR activity, we found that inhibition of PKC-3 activity in P1 led to the failure of pPARs to polarize (Figure 5A), similar to what we observed previously when using a small molecule inhibitor.[20]

To test if accumulation of PAR-3 at the cell contact by furrow flows is required for early pPAR polarization away from the contact, we used the oligomerization defective PAR-3(Δ69-82) mutant, which is defective in its ability to segregate with cortical flows.[25,26,28,29] We found that PAR-3(Δ69-82) failed to accumulate to detectable levels at the cell contact (Figure 5B), and PAR-2 invariably failed to clear from the cell contact in these mutants (Figure 5C). In ~20% of the cases, this defect in polarization led to the failure of asymmetric PAR-2 inheritance between P2 and EMS at the 4-cell stage (Figure 5D). Thus, consistent with our model, failure to accumulate PAR-3 at the nascent cell contact is associated with defects in P1 polarity.

Given the established role of cell contacts in orienting polarity in other systems, including P2 and P3 blastomeres of the *C. elegans* germline,[30] we next asked whether the cell contact might have an instructive role in orienting polarity in P1. If this were the case, then the cell contact should provide a persistent cue to orient the polarity axis, thereby reorienting any misaligned domains to the embryo long axis (Figure 5E). To perturb the orientation of PAR domains in P1, we turned to focused light-induced cytoplasmic streaming (FLUCS), which has been shown to be capable of rotating PAR domains in the zygote.[31] Note that we used *nmy-2(ts)* embryos in these experiments to suppress any PAR-dependent induction of actomyosin flows that could stabilize domain orientation, as is seen in the zygote.[13] By applying FLUCS in P1 for 5 min following completion of cytokinesis, we were able to reliably rotate the PAR domains in P1 such that they were no longer properly oriented with respect to the cell contact (Figure 5F). Surprisingly, we found that the misaligned PAR domains persisted through to anaphase (~8.5 min) (Figures 5F and 5G), arguing against a persistent polarity cue originating at the cell contact.

Accumulation of aPARs at the cleavage furrow can induce mirror-symmetric polarity in symmetrically dividing cells

Finally, we asked whether furrow flows could more broadly drive *de novo* polarization, independently of the specific fate and polarity inherited by P1. Specifically, we hypothesized that in the context of symmetric cell divisions, furrow-induced flows would localize PAR-3 centrally at the contact site, which should in turn restrict PAR-2 localization toward the outer poles to yield so-called mirror-symmetric polarity in daughter cells. Such a result would suggest that furrow flows could provide a simple and generalizable mechanism for linking polarity to cell division.

To test this idea, we suppressed polarization of zygotes by inhibiting PKC-3AS, which divided to yield pairs of symmetric daughter cells.[27] By washing out 1NA-PP1 during furrow closure in zygotes, we could then reactivate PKC-3 activity in the daughter cells and follow polarization (Figures 6 and S6; Video S4). We found that clusters of PAR-3 molecules moved inward with the ingressing furrow membranes during cytokinesis (Figure 6B; Video S4), leading to enrichment of PAR-3 at the nascent cell contact (Figures 6 and S6). The resulting symmetric daughter cell pairs then invariably developed mirror-symmetric polarity, with PAR-2 segregating away from the nascent division site (Figures 6 and S6). Consistent with our model, mirror-symmetric polarization failed either if PKC-3 activity was inhibited in the daughter cells or if we reduced the ability of PAR-3 to accumulate at the cell contact (PAR-3(Δ69-82)) (Figure 6). This ability to disconnect cell fate from the capacity for cells to polarize may also explain why AB cells that inherit excess PAR-2 relative to aPARs tend to polarize away from the cell contact.[32]

This ability of furrow flows to link polarity to cell division independently of prior positional information and cell fate identity support its role as a general physical mechanism for controlling cell organization in actively dividing systems and could contribute to the generation of mirror-symmetric polarized cells in diverse developmental contexts.[33–35]

DISCUSSION

Coupling between division and polarity is important for coordinating cellular geometry in actively dividing tissues.[36] Although the role of cell polarity in orienting cell divisions is well established,[37] it is increasingly clear that the reverse is also true. This ability of cell division to orient polarity has been linked to a

Figure 4. Furrow direct flows establish a persistent pool of aPARs that marks the anterior of P1

(A) Time course of photobleaching protocol used to isolate P1 membrane signal as applied to a generic plasma membrane marker, PH-PLC1d1 (n = 6). Dashed box indicates the photobleached region. See also Figure S5.

(B) Confocal images of pre- (0′) and post-recovery (0.5′, 3′) embryos expressing mNG::PAR-3 (NWG0189) (n = 8) and mNG::PAR-3(S950A) (NWG0259) (n = 6). Yellow arrows indicate that molecules that accumulate toward the leading edge of the closing furrow directly lead to a corresponding enrichment at the P1 cell contact post-cytokinesis.

(C) (Left) A schematic and midsection confocal image showing localizations of mNG::PAR-2 (LP637) and mNG::PAR-2 (S241A; 4mer) (NWG0473) in the zygote. (Right) Representative examples of embryos expressing mNG::PAR-2 (S241A; 4mer) (NWG0473) (n = 7) as in (B).

(D) (Left) A schematic of the quantification protocol is shown. (Right) Quantification of membrane profiles from embryos corresponding to conditions shown in (A)–(C). Profiles were normalized by intensity and distance. Mean and 95% confidence interval (bootstrapped) indicated.

(E) (Left) Representative examples of embryos expressing PAR-6::mNG (LP216) (n = 7) as in (B) and (C). (Right) Quantification of the corresponding membrane distributions 3 min post-recovery. Dashed arrow indicates region quantified.

Scale bars (A–E), 20 μm.

See also Figure S5 and Video S3.

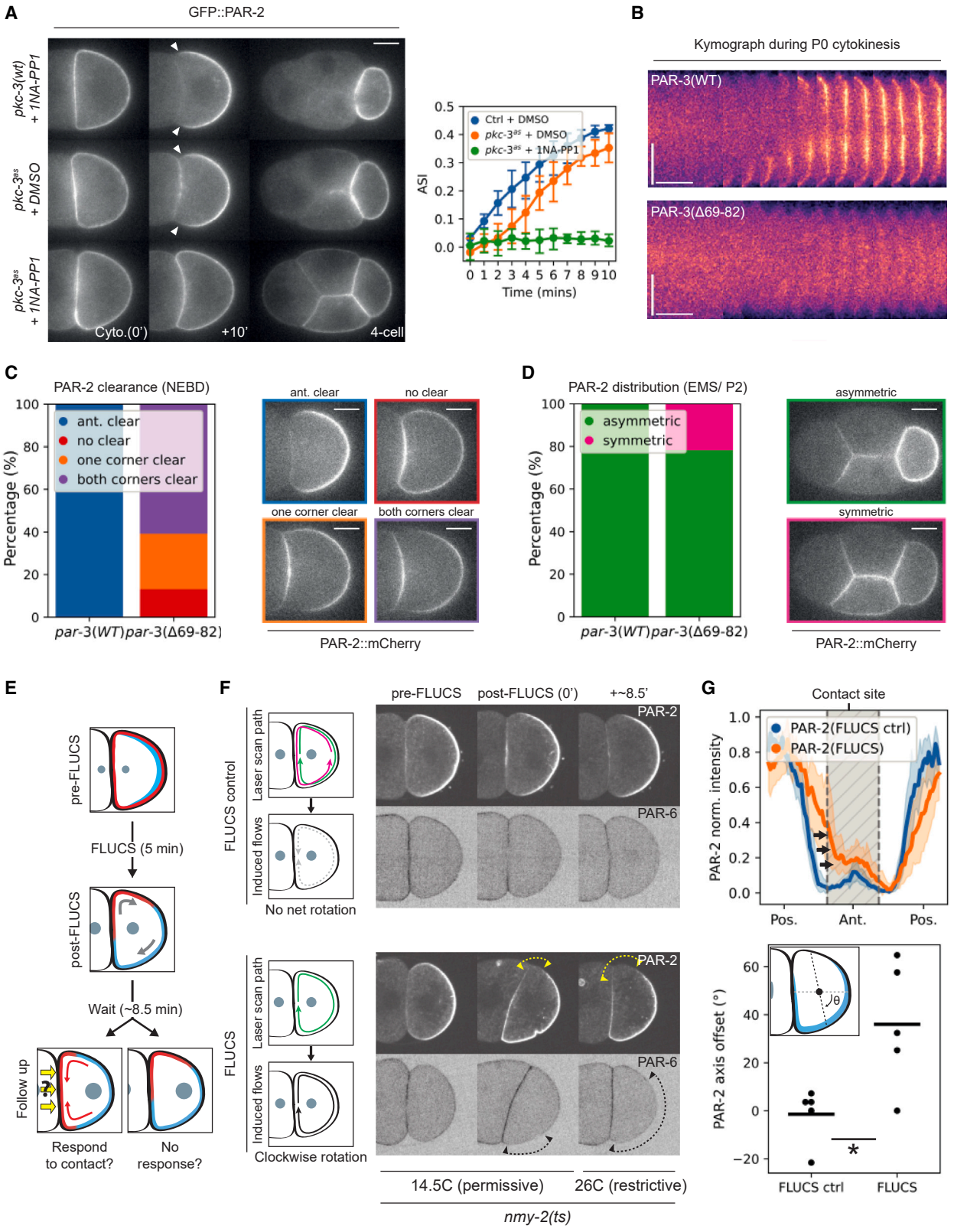

(legend on next page)

variety of spatial cues, including cytokinesis remnants, the spindle midzone, the midbody, and/or contact-dependent signaling between newly generated daughter cells.[38–47] In many of these cases, polarization is associated with the accumulation of polarity-related molecules, including PAR-3, within the cleavage furrow, midbody, and/or nascent contact site.[33,35,39,47,48]

Here, we show that furrow-directed flows provide a simple physical mechanism to achieve targeting of polarity proteins to the nascent cell contact. Our data suggest that in P1, enrichment of PAR-3 at the cell contact by furrow-directed flows acts as the first step in PAR polarization, which then biases downstream polarity pathways to orient the polarity axis. Consistent with this model, polarization requires phosphorylation of pPARs by PKC-3 and is compromised when we use a monomeric variant of PAR-3 that exhibits reduced accumulation in the furrow. Our data argue against an instructive role of the cell contact, at least for the initial symmetry-breaking event that drives PAR-2 segregation. Most notably, misaligned PAR domains fail to re-orient with respect to the cell contact. In addition, the observation that PAR-2 still polarizes away from cell contacts in blastomeres in which fate specification is disrupted (Figures 6 and S4F) indicates that cell identity and fate-dependent signaling between cells is not essential. These results are generally consistent with observations that AB and its descendants are unable to orient polarity or the spindle when placed in contact with P lineage blastomeres,[30,49] as well as the fact that contact-dependent polarity cues in the early embryo, where they exist, tend to orient PAR-2 toward (and aPARs away from) cell contacts.[30,50]

We therefore propose that PAR polarization in P1 (Figure 7) proceeds as follows: first, early cleavage furrow-directed cortical flows advect PAR-3 to drive accumulation of a pool of aPARs at the nascent cell contact, marking the putative anterior. Outside of this selective enrichment, aPAR membrane concentrations are initially low throughout the rest of the cell, whereas pPARs are uniformly high (Figure 7). Next, biased by aPARs at the cell contact, PAR-2 self-organization drives the timely formation of a posterior pPAR domain. Concurrently, despite an initial asymmetry, aPARs load progressively throughout the plasma membrane of P1, leading to overlap between aPARs and pPARs at the posterior. Finally, pPAR-dependent exclusion of aPARs and late cortical flows combine to drive bulk segregation of aPARs into a visible anterior domain, resulting in the characteristic mutually exclusive distributions of aPARs and pPARs. Thus, despite overt differences in the pattern of polarization between the zygote and P1, there appears to be remarkable conservation in the polarity pathways, including the use of cortical flows as the earliest symmetry-breaking cue. Instead, the key difference lies in the source of these actomyosin flows. Whereas zygotes utilize centrosome-induced flows to provide a cell-autonomous cue, P1 harnesses furrow flows associated with the previous cell division to enable coordination of polarity with AB.

Although technical limitations prevented more extensive analysis in P2, our data suggest that this basic picture is preserved (Figure S7). Notably, in addition to polarity being sensitive to disruption of late cortical flows and aPAR exclusion by pPARs (Figure S7B), we also found that PAR-2 was initially biased away from the contact site as in P1, before eventually reversing due to the signaling from neighboring cells. This observation suggests that the furrow-associated cue is also active but ultimately overridden by MES-1/SRC-1 signaling in P2 to reverse polarity[30] (Figure S7C).

That said, it is difficult to fully exclude the existence of additional guiding cues that could help refine polarity and compensate for early defects in furrow-dependent polarization. Indeed, even though P1 blastomeres from *par-3(Δ69-82)* embryos exhibited defects in symmetry-breaking, the majority were still able to undergo asymmetric division, at least with respect to asymmetric inheritance of PAR-2 by the daughter cells. Co-enrichment of other signaling molecules with PAR-3 in the furrow[48,51] or even the midbody[40,47] could provide additional cues, and we cannot exclude the possibility that the late cortical flows we observe may be biased by other signals,[21] which could rescue initial defects in the furrow-dependent pathway we describe. The use of multiple complementary cues to polarize is common in many systems, including the *C. elegans* zygote,[12,52,53] and it would not be surprising if the same were true in P1.[21]

Given the ubiquity of furrow-directed flows in dividing cells,[54–57] advection of molecules into the nascent furrow is likely to be a common strategy to coordinate molecular asymmetries with the division axis. Such flows have been proposed to promote efficient cytokinesis by concentrating actomyosin regulators within the furrow.[58,59] With this work, we show that furrow-dependent flows can also play a role in coordinating intracellular patterning, which helps to ensure proper cell and tissue organization in dynamic, actively dividing systems.

STAR★METHODS

Detailed methods are provided in the online version of this paper and include the following:

Figure 5. Enrichment of aPAR activity at the contact biases the orientation of pPAR polarization

(A) (Left) A time series of midsection confocal images of embryos expressing GFP::PAR-2 in a PKC-3(WT) (KK1273) (n = 5), or PKC-3AS background (NWG0316), and treated with DMSO (n = 5) or 20 μM of the ATP analog 1NA-PP1 (n = 5). Arrowheads indicate PAR-2 clearance from the cell anterior. (Right) Quantification of asymmetry index (ASI) for times indicated for the corresponding conditions. Mean and 95% confidence interval (bootstrapped) indicated.

(B) Kymograph of embryos expressing mCherry::PAR-2 (not shown) with either mNG::PAR-3 (NWG0458) or mNG::PAR-3(Δ69-82) (NWG0397), during furrow closure of the zygote. Scale bars, vertical, 10 μm; horizontal, 1 min.

(C and D) Distribution of PAR-2 localization phenotypes with representative midsection confocal images during NEBD (C), or at the 4-cell stage (D) for conditions corresponding to (B). Sample sizes, *par-3(wt)* embryos (n = 12) and par-3(Δ69-82) embryos (n = 24).

(E) Schematic of FLUCS setup to test if P1 polarity axis responds to contact signaling.

(F) Midsection confocal images of embryos expressing GFP::PAR-2 and PAR-6::mCherry in an *nmy-2(ts)* background (NWG0283) at indicated times subjected to the FLUCS setup in (E). Yellow and black arrowheads with dashed lines indicate misaligned regions of PAR-2 and PAR-6 clearance, respectively.

(G) Quantification of PAR-2 membrane distributions (top) and PAR-2 domain axis relative to the cell contact (bottom) post-FLUCS (~8.5 min) for conditions corresponding to (F). Arrows indicate the shift in PAR-2 membrane distributions relative to the contact site in FLUCS conditions. * p value < 0.05, students t test, unpaired, two tailed.

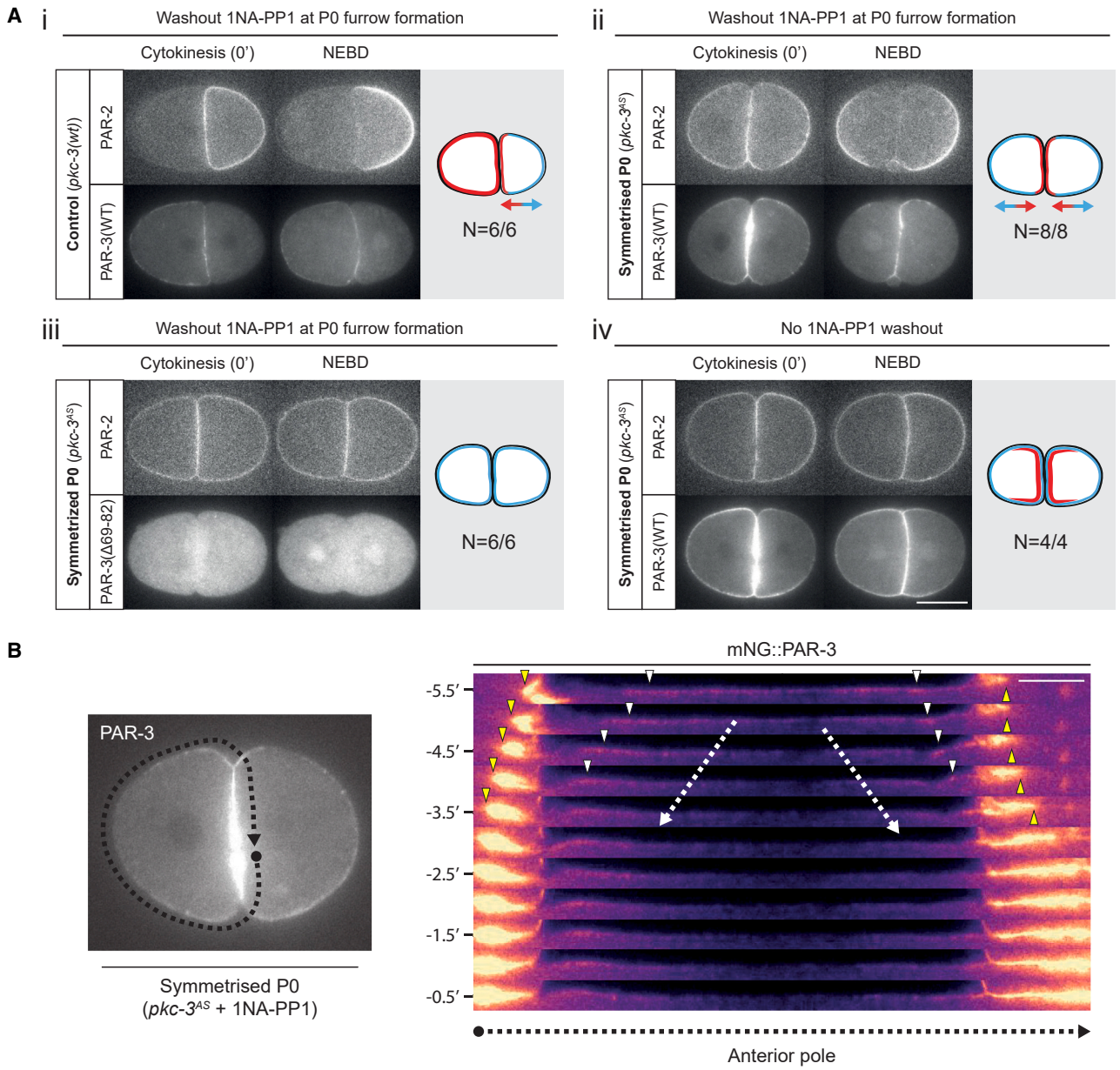

Figure 6. Advection of PAR-3 by furrow-directed flows can induce mirror-symmetric polarization in symmetric daughter cell pairs

(A) Time series of midsection confocal images of embryos at indicated time points expressing mCherry::PAR-2 with either (i) mNG::PAR-3(WT) and PKC-3(WT) (NWG0453), or (ii) mNG::PAR-3(WT) and PKC-3AS (NWG0458), or (iii) mNG::PAR-3(Δ69-82) and PKC-3AS (NWG0526), when the zygote is treated with 100 μM 1NA-PP1, and washed out during furrow formation (i–iii) or with no buffer exchange as a control (iv). Schematics of the resulting polarity shown at right, graded arrows indicate orientation of PAR polarity, aPARs are labeled as red, and pPARs as cyan. Scale bar, 20 μm.

(B) Kymograph of PAR-3 distributions for the indicated ROI (dashed line with arrowhead) during cytokinesis following washout of 1NA-PP1 in a symmetrized PKC-3AS embryo (the same embryo shown in (Aii). Note that PAR-3 flows toward the leading edge of the forming furrow (white arrowheads), leading to clearance of PAR-3 from the pole and accumulation of PAR-3 at the leading edge (yellow arrowheads). Time relative to cytokinesis completion (0′). Scale bar, 10 μm.

See also Figure S6 and Video S4.

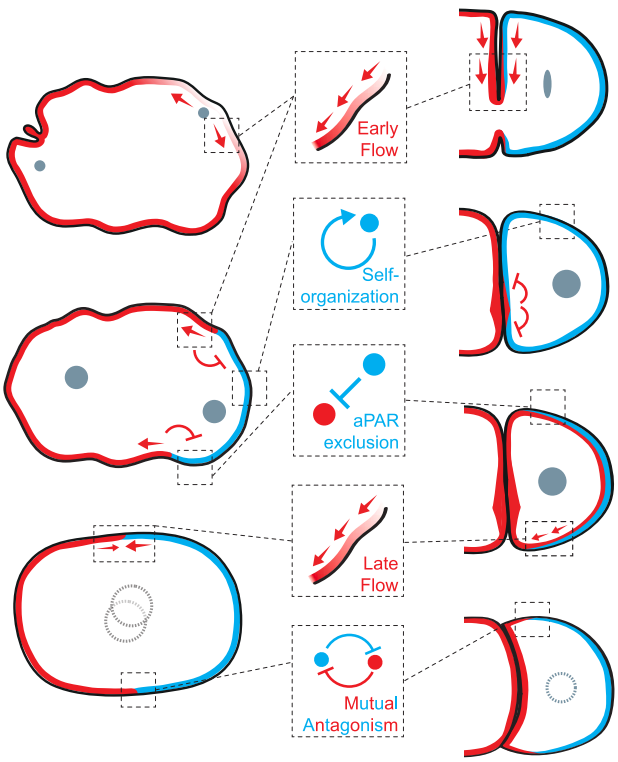

Figure 7. Comparison of PAR polarization in the zygote and P1 blastomere

Comparison of models for PAR polarization between the zygote and P1. (Left) In the zygote, prior to symmetry breaking (SB), aPARs are initially enriched on the cortex. SB is triggered by centrosomes, which induce early cortical flows that segregate aPARs to the anterior, allowing pPARs to load at the posterior. Biased either by asymmetry of aPARs or aPAR activity (i.e., local protection of PAR-2 from PKC-3 activity by microtubules), PAR-2 self-organization at the posterior helps to form and stabilize a posterior pPAR domain, which further promotes exclusion of aPARs from the posterior. By mitosis, aPARs and pPARs display mutually exclusive localizations, which are maintained via mutual antagonism. The boundaries of each PAR domain are also stabilized by late cortical flows, which are directed toward the midline. (Right) During P0 cytokinesis, early cleavage furrow-directed flows lead to accumulation of PAR-3 at the leading edge, which concentrates PAR-3 at the nascent cell contact (anterior) of P1. By completion of P0 cytokinesis, these early flows cease, leading to low aPAR levels across the membrane of the cell apart from enrichment at the cell contact. By contrast, pPARs are initially uniformly distributed throughout P1. Soon after, biased by the accumulation of aPARs at the contact (anterior) by early furrow flows, pPARs polarize away from the anterior, which is facilitated by PAR-2 self-organization for timely formation of a pPAR domain. Concurrently, aPARs load throughout the cell, resulting in overlap of aPARs and pPARs at the posterior. Finally, late flows and posterior exclusion of aPARs by pPARs segregates aPARs toward the anterior, resulting in the stereotyped mutually exclusive localization of aPARs and pPARs.
See also Figure S7.

  - Imaging – live imaging
  - Imaging – laser ablation
  - Imaging – FLUCS
- QUANTIFICATION AND STATISTICAL ANALYSIS
  - Image analysis - particle image velocimetry
  - Image analysis – quantification of membrane profile
  - Image analysis – defining anterior and posterior poles in the zygote
  - Image analysis – alignment of time series data in P1
  - Image analysis – ASI
  - Image analysis – domain size
  - Image analysis – particle detection and tracking
  - Statistics

SUPPLEMENTAL INFORMATION

Supplemental information can be found online at https://doi.org/10.1016/j.cub.2023.08.076.

ACKNOWLEDGMENTS

We thank Nic Tapon, Clare Buckley, and the Goehring Lab for comments on the manuscript and Lesilee Rose for discussions of unpublished data. Some strains were provided by the Caenorhabditis Genome Center (CGC), which is funded by the NIH Office of Research Infrastructure Programs (P40 OD010440). FLUCS experiments were performed in the Light Microscopy Facility at the MPI-CBG with support from Britta Schroth-Diez, Romina Piscitello, and the Kreysing and Hyman Labs. This work was supported by the Francis Crick Institute (N.W.G.), which receives its core funding from Cancer Research UK (CC2119), the UK Medical Research Council (CC2119), and the Wellcome Trust (CC2119). M.K. acknowledges funding by the Max Planck Society, the Karlsruhe Institute of Technology, the European Research Council (grant no. 853619), the Hector Foundation, and the Deutsche Forschungsgemeinschaft (DFG, German Research Foundation) under Germany's Excellence Strategy – 2082/1 – 390761711.

AUTHOR CONTRIBUTIONS

Conceptualization, K.N. and N.W.G.; methodology, K.N., S.W., and M.K.; formal analysis, K.N.; investigation, K.N.; resources, K.N., N.H., T.B., and J.B.-P.; writing – original draft preparation, K.N. and N.W.G.; writing – review and editing, K.N., N.H., T.B., J.B.-P., S.W., M.K., and N.W.G.; supervision, M.K. and N.W.G.; project administration, M.K. and N.W.G.; funding acquisition, M.K. and N.W.G.

DECLARATION OF INTERESTS

M.K. filed European and worldwide patents for FLUCS technology and acts as a consultant to Rapp OptoElectronic.

INCLUSION AND DIVERSITY

We support inclusive, diverse, and equitable conduct of research. One or more of the authors of this paper received support from a program designed to increase minority representation in their field of research.

Received: January 24, 2023
Revised: July 13, 2023
Accepted: August 24, 2023
Published: September 19, 2023

REFERENCES

1. Rose, L., and Gönczy, P. (2014). Polarity establishment, asymmetric division and segregation of fate determinants in early *C. elegans* embryos. WormBook, 1–43.
2. Sulston, J.E., Schierenberg, E., White, J.G., and Thomson, J.N. (1983). The embryonic cell lineage of the nematode *Caenorhabditis elegans*. Dev. Biol. *100*, 64–119.
3. Beatty, A., Morton, D., and Kemphues, K. (2010). The *C. elegans* homolog of Drosophila Lethal giant larvae functions redundantly with PAR-2 to maintain polarity in the early embryo. Development *137*, 3995–4004.
4. Boyd, L., Guo, S., Levitan, D., Stinchcomb, D.T., and Kemphues, K.J. (1996). PAR-2 is asymmetrically distributed and promotes association of

P granules and PAR-1 with the cortex in *C. elegans* embryos. Development *122*, 3075–3084.

5. Etemad-Moghadam, B., Guo, S., and Kemphues, K.J. (1995). Asymmetrically distributed PAR-3 protein contributes to cell polarity and spindle alignment in early *C. elegans* embryos. Cell *83*, 743–752.
6. Gotta, M., Abraham, M.C., and Ahringer, J. (2001). CDC-42 controls early cell polarity and spindle orientation in *C. elegans*. Curr. Biol. *11*, 482–488.
7. Guo, S., and Kemphues, K.J. (1995). *par-1*, a gene required for establishing polarity in *C. elegans* embryos, encodes a putative Ser/Thr kinase that is asymmetrically distributed. Cell *81*, 611–620.
8. Hoege, C., Constantinescu, A.T., Schwager, A., Goehring, N.W., Kumar, P., and Hyman, A.A. (2010). LGL can partition the cortex of one-cell *Caenorhabditis elegans* embryos into two domains. Curr. Biol. *20*, 1296–1303.
9. Kumfer, K.T., Cook, S.J., Squirrell, J.M., Eliceiri, K.W., Peel, N., O'Connell, K.F., and White, J.G. (2010). CGEF-1 and CHIN-1 regulate CDC-42 activity during asymmetric division in the *Caenorhabditis elegans* embryo. Mol. Biol. Cell *21*, 266–277.
10. Tabuse, Y., Izumi, Y., Piano, F., Kemphues, K.J., Miwa, J., and Ohno, S. (1998). Atypical protein kinase C cooperates with PAR-3 to establish embryonic polarity in *Caenorhabditis elegans*. Development *125*, 3607–3614.
11. Watts, J.L., Etemad-Moghadam, B., Guo, S., Boyd, L., Draper, B.W., Mello, C.C., Priess, J.R., and Kemphues, K.J. (1996). *par-6*, a gene involved in the establishment of asymmetry in early *C. elegans* embryos, mediates the asymmetric localization of PAR-3. Development *122*, 3133–3140.
12. Motegi, F., Zonies, S., Hao, Y., Cuenca, A.A., Griffin, E., and Seydoux, G. (2011). Microtubules induce self-organization of polarized PAR domains in *Caenorhabditis elegans* zygotes. Nat. Cell Biol. *13*, 1361–1367.
13. Sailer, A., Anneken, A., Li, Y., Lee, S., and Munro, E. (2015). Dynamic opposition of clustered proteins stabilizes cortical polarity in the *C. elegans* zygote. Dev. Cell *35*, 131–142.
14. Cowan, C.R., and Hyman, A.A. (2004). Asymmetric cell division in *C. elegans*: cortical polarity and spindle positioning. Annu. Rev. Cell Dev. Biol. *20*, 427–453.
15. Schonegg, S., and Hyman, A.A. (2006). CDC-42 and RHO-1 coordinate acto-myosin contractility and PAR protein localization during polarity establishment in *C. elegans* embryos. Development *133*, 3507–3516.
16. Goehring, N.W., Trong, P.K., Bois, J.S., Chowdhury, D., Nicola, E.M., Hyman, A.A., and Grill, S.W. (2011). Polarization of PAR proteins by advective triggering of a pattern-forming system. Science *334*, 1137–1141.
17. Munro, E., Nance, J., and Priess, J.R. (2004). Cortical flows powered by asymmetrical contraction transport PAR proteins to establish and maintain anterior-posterior polarity in the early *C. elegans* embryo. Dev. Cell *7*, 413–424.
18. Arata, Y., Hiroshima, M., Pack, C.G., Ramanujam, R., Motegi, F., Nakazato, K., Shindo, Y., Wiseman, P.W., Sawa, H., Kobayashi, T.J., et al. (2016). Cortical polarity of the RING protein PAR-2 is maintained by exchange rate kinetics at the cortical-cytoplasmic boundary. Cell Rep. *16*, 2156–2168.
19. Hao, Y., Boyd, L., and Seydoux, G. (2006). Stabilization of cell polarity by the *C. elegans* RING protein PAR-2. Dev. Cell *10*, 199–208.
20. Hubatsch, L., Peglion, F., Reich, J.D., Rodrigues, N.T., Hirani, N., Illukkumbura, R., and Goehring, N.W. (2019). A cell size threshold limits cell polarity and asymmetric division potential. Nat. Phys. *15*, 1075–1085.
21. Koch, L.A., and Rose, L.S. (2023). Multiple pathways for reestablishing PAR polarity in *C. elegans* embryo. Dev. Biol. *500*, 40–54.
22. Cuenca, A.A., Schetter, A., Aceto, D., Kemphues, K., and Seydoux, G. (2003). Polarization of the *C. elegans* zygote proceeds via distinct establishment and maintenance phases. Development *130*, 1255–1265.
23. Liu, J., Maduzia, L.L., Shirayama, M., and Mello, C.C. (2010). NMY-2 maintains cellular asymmetry and cell boundaries, and promotes a SRC-dependent asymmetric cell division. Dev. Biol. *339*, 366–373.
24. Pittman, K.J., and Skop, A.R. (2012). Anterior PAR proteins function during cytokinesis and maintain DYN-1 at the cleavage furrow in *Caenorhabditis elegans*. Cytoskeleton (Hoboken) *69*, 826–839.
25. Illukkumbura, R., Hirani, N., Borrego-Pinto, J., Bland, T., Ng, K., Hubatsch, L., McQuade, J., Endres, R.G., and Goehring, N.W. (2023). Design principles for selective polarization of PAR proteins by cortical flows. J. Cell Biol. *222*, e202209111.
26. Rodriguez, J., Peglion, F., Martin, J., Hubatsch, L., Reich, J., Hirani, N., Gubieda, A.G., Roffey, J., Fernandes, A.R., St Johnston, D., et al. (2017). aPKC cycles between functionally distinct PAR protein assemblies to drive cell polarity. Dev. Cell *42*, 400–415.e9.
27. Ng, K., Bland, T., Hirani, N., and Goehring, N.W. (2022). An analog sensitive allele permits rapid and reversible chemical inhibition of PKC-3 activity in *C. elegans*. MicroPubl. Biol. https://doi.org/10.17912/micropub.biology.000610.
28. Chang, Y., and Dickinson, D.J. (2022). A particle size threshold governs diffusion and segregation of PAR-3 during cell polarization. Cell Rep. *39*, 110652.
29. Dickinson, D.J., Schwager, F., Pintard, L., Gotta, M., and Goldstein, B. (2017). A single-cell biochemistry approach reveals PAR complex dynamics during cell polarization. Dev. Cell *42*, 416–434.e11.
30. Arata, Y., Lee, J.Y., Goldstein, B., and Sawa, H. (2010). Extracellular control of PAR protein localization during asymmetric cell division in the *C. elegans* embryo. Development *137*, 3337–3345.
31. Mittasch, M., Gross, P., Nestler, M., Fritsch, A.W., Iserman, C., Kar, M., Munder, M., Voigt, A., Alberti, S., Grill, S.W., et al. (2018). Non-invasive perturbations of intracellular flow reveal physical principles of cell organization. Nat. Cell Biol. *20*, 344–351.
32. Lim, Y.W., Wen, F.L., Shankar, P., Shibata, T., and Motegi, F. (2021). A balance between antagonizing PAR proteins specifies the pattern of asymmetric and symmetric divisions in *C. elegans* embryogenesis. Cell Rep. *36*, 109326.
33. Buckley, C.E., Ren, X., Ward, L.C., Girdler, G.C., Araya, C., Green, M.J., Clark, B.S., Link, B.A., and Clarke, J.D. (2013). Mirror-symmetric microtubule assembly and cell interactions drive lumen formation in the zebrafish neural rod. EMBO J. *32*, 30–44.
34. Symonds, A.C., Buckley, C.E., Williams, C.A., and Clarke, J.D.W. (2020). Coordinated assembly and release of adhesions builds apical junctional belts during de novo polarisation of an epithelial tube. Development *147*, dev191494.
35. Tawk, M., Araya, C., Lyons, D.A., Reugels, A.M., Girdler, G.C., Bayley, P.R., Hyde, D.R., Tada, M., and Clarke, J.D. (2007). A mirror-symmetric cell division that orchestrates neuroepithelial morphogenesis. Nature *446*, 797–800.
36. Buckley, C.E., and St Johnston, D. (2022). Apical–basal polarity and the control of epithelial form and function. Nat. Rev. Mol. Cell Biol. *23*, 559–577.
37. Goldstein, B., and Macara, I.G. (2007). The PAR proteins: fundamental players in animal cell polarization. Dev. Cell *13*, 609–622.
38. Etienne-Manneville, S. (2004). Cdc42-the centre of polarity. J. Cell Sci. *117*, 1291–1300.
39. Harris, K.P., and Tepass, U. (2010). Cdc42 and vesicle trafficking in polarized cells. Traffic *11*, 1272–1279.
40. Li, D., Mangan, A., Cicchini, L., Margolis, B., and Prekeris, R. (2014). FIP5 phosphorylation during mitosis regulates apical trafficking and lumenogenesis. EMBO Rep. *15*, 428–437.
41. Luján, P., Varsano, G., Rubio, T., Hennrich, M.L., Sachsenheimer, T., Gálvez-Santisteban, M., Martín-Belmonte, F., Gavin, A.C., Brügger, B., and Köhn, M. (2016). PRL-3 disrupts epithelial architecture by altering the post-mitotic midbody position. J. Cell Sci. *129*, 4130–4142.
42. Meitinger, F., Khmelinskii, A., Morlot, S., Kurtulmus, B., Palani, S., Andres-Pons, A., Hub, B., Knop, M., Charvin, G., and Pereira, G. (2014). A memory system of negative polarity cues prevents replicative aging. Cell *159*, 1056–1069.

43. Miller, K.E., Kang, P.J., and Park, H.O. (2020). Regulation of Cdc42 for polarized growth in budding yeast. Microb. Cell *7*, 175–189.
44. Pollarolo, G., Schulz, J.G., Munck, S., and Dotti, C.G. (2011). Cytokinesis remnants define first neuronal asymmetry in vivo. Nat. Neurosci. *14*, 1525–1533.
45. Rathbun, L.I., Colicino, E.G., Manikas, J., O'Connell, J., Krishnan, N., Reilly, N.S., Coyne, S., Erdemci-Tandogan, G., Garrastegui, A., Freshour, J., et al. (2020). Cytokinetic bridge triggers de novo lumen formation in vivo. Nat. Commun. *11*, 1269.
46. Schlüter, M.A., Pfarr, C.S., Pieczynski, J., Whiteman, E.L., Hurd, T.W., Fan, S., Liu, C.J., and Margolis, B. (2009). Trafficking of Crumbs3 during cytokinesis is crucial for lumen formation. Mol. Biol. Cell *20*, 4652–4663.
47. Wang, T., Yanger, K., Stanger, B.Z., Cassio, D., and Bi, E. (2014). Cytokinesis defines a spatial landmark for hepatocyte polarization and apical lumen formation. J. Cell Sci. *127*, 2483–2492.
48. Liang, X., Weberling, A., Hii, C.Y., Zernicka-Goetz, M., and Buckley, C.E. (2022). E-cadherin mediates apical membrane initiation site localisation during de novo polarisation of epithelial cavities. EMBO J. *41*, e111021.
49. Sugioka, K., and Bowerman, B. (2018). Combinatorial contact cues specify cell division orientation by directing cortical myosin flows. Dev. Cell *46*, 257–270.e5.
50. Anderson, D.C., Gill, J.S., Cinalli, R.M., and Nance, J. (2008). Polarization of the *C. elegans* embryo by RhoGAP-mediated exclusion of PAR-6 from cell contacts. Science *320*, 1771–1774.
51. Naturale, V.F., Pickett, M.A., and Feldman, J.L. (2023). Persistent cell contacts enable E-cadherin/HMR-1- and PAR-3-based symmetry breaking within a developing C. elegans epithelium. Dev. Cell *58*, 1–17.
52. Gross, P., Kumar, K.V., Goehring, N.W., Bois, J.S., Hoege, C., Jülicher, F., and Grill, S.W. (2019). Guiding self-organized pattern formation in cell polarity establishment. Nat. Phys. *15*, 293–300.
53. Klinkert, K., Levernier, N., Gross, P., Gentili, C., von Tobel, L., Pierron, M., Busso, C., Herrman, S., Grill, S.W., Kruse, K., et al. (2019). Aurora A depletion reveals centrosome-independent polarization mechanism in *Caenorhabditis elegans*. eLife *8*, e44552.
54. Bray, D., and White, J.G. (1988). Cortical flow in animal cells. Science *239*, 883–888.
55. Cao, L.G., and Wang, Y.L. (1990). Mechanism of the formation of contractile ring in dividing cultured animal cells. II. Cortical movement of microinjected actin filaments. J. Cell Biol. *111*, 1905–1911.
56. Chen, W., Foss, M., Tseng, K.F., and Zhang, D. (2008). Redundant mechanisms recruit actin into the contractile ring in silkworm spermatocytes. PLoS Biol. *6*, e209.
57. Yumura, S. (2001). Myosin II dynamics and cortical flow during contractile ring formation in *Dictyostelium* cells. J. Cell Biol. *154*, 137–146.
58. Khaliullin, R.N., Green, R.A., Shi, L.Z., Gomez-Cavazos, J.S., Berns, M.W., Desai, A., and Oegema, K. (2018). A positive-feedback-based mechanism for constriction rate acceleration during cytokinesis in *Caenorhabditis elegans*. eLife *7*, e36073.
59. Longhini, K.M., and Glotzer, M. (2022). Aurora A and cortical flows promote polarization and cytokinesis by inducing asymmetric ECT-2 accumulation. eLife *11*, e83992.
60. Rodrigues, N.T.L., Bland, T., Borrego-Pinto, J., Ng, K., Hirani, N., Gu, Y., Foo, S., and Goehring, N.W. (2022). SAIBR: a simple, platform-independent method for spectral autofluorescence correction. Development *149*, dev200545.
61. Thielicke, W., and Stamhuis, E.J. (2014). PIVlab – towards user-friendly, affordable and accurate digital particle image velocimetry in MATLAB. J. Open Res. Softw. *2*, e30.
62. Schindelin, J., Arganda-Carreras, I., Frise, E., Kaynig, V., Longair, M., Pietzsch, T., Preibisch, S., Rueden, C., Saalfeld, S., Schmid, B., et al. (2012). Fiji: an open-source platform for biological-image analysis. Nat. Methods *9*, 676–682.
63. Allan, D.B., Caswell, T., Keim, N.C., and van der Wel, C.M. (2018). trackpy: Trackpy v0.4.1 (v0.4.1)(Zenodo). https://doi.org/10.5281/zenodo.1226458.
64. Stiernagle, T. (2006). Maintenance of *C. elegans*. WormBook, 1–11.
65. Arribere, J.A., Bell, R.T., Fu, B.X., Artiles, K.L., Hartman, P.S., and Fire, A.Z. (2014). Efficient marker-free recovery of custom genetic modifications with CRISPR/Cas9 in *Caenorhabditis elegans*. Genetics *198*, 837–846.
66. Kamath, R.S., and Ahringer, J. (2003). Genome-wide RNAi screening in *Caenorhabditis elegans*. Methods *30*, 313–321.
67. Edgar, L.G., and Goldstein, B. (2012). Culture and manipulation of embryonic cells. Methods Cell Biol. *107*, 151–175.
68. Goehring, N.W., Hoege, C., Grill, S.W., and Hyman, A.A. (2011). PAR proteins diffuse freely across the anterior–posterior boundary in polarized *C. elegans* embryos. J. Cell Biol. *193*, 583–594.
69. Pimpale, L.G., Middelkoop, T.C., Mietke, A., and Grill, S.W. (2020). Cell lineage-dependent chiral actomyosin flows drive cellular rearrangements in early *Caenorhabditis elegans* development. eLife *9*, e54930.
70. Reich, J.D., Hubatsch, L., Illukkumbura, R., Peglion, F., Bland, T., Hirani, N., and Goehring, N.W. (2019). Regulated activation of the PAR polarity network ensures a timely and specific response to spatial cues. Curr. Biol. *29*, 1911–1923.e5.

STAR★METHODS

KEY RESOURCES TABLE

REAGENT or RESOURCE	SOURCE	IDENTIFIER
Bacterial and virus strains		
E. coli: OP50: E. coli B, uracil auxotroph	CGC	WB Strain: OP50
E. coli: HT115(DE3): F-, mcrA, mcrB, IN(rrnD-rrnE)1, rnc14::Tn10(DE3 lysogen: lavUV5 promoter-T7 polymerase).	CGC	WB Strain: HT115(DE3)
Chemicals, peptides, and recombinant proteins		
Chemically defined lipid concentrate	ThermoFisher	11905031
PP1 Analog, 1NA-PP1	Merck	529579
Nocodazole	Merck	M1404
Latrunculin A	Enzo	BML-T119-0100
Alt-R™ S.p. Cas9 Nuclease V3	IDT	1081058
Alt-R® CRISPR-Cas9 tracrRNA	IDT	1072532
Experimental models: Organisms/strains		
C. elegans: BOX241: *par-6(mib25[par-6::mCherry-LoxP]) I*	Mike Boxem	BOX241
C. elegans: KK1254: *par-2(it315[mCherry::par-2]) III*	Ken Kempheus	WB Strain: KK1254
C. elegans: KK1273: *par-2(it328[GFP::par-2]) III*	CGC/Ken Kempheus	WB Strain: KK1273
C. elegans: LP162: *nmy-2(cp13[nmy-2::gfp + LoxP]) I*	CGC	WB Strain: LP162
C. elegans: LP216: *par-6(cp45[par-6::mNeonGreen::3xFlag + LoxP unc-119(+) LoxP]) I; unc-119(ed3) III*	Dan Dickinson	WB Strain: LP216
C. elegans: LP637: *par-2(cp329[mNG::par-2]) III*	Dan Dickinson	WB Strain: LP637
C. elegans: N2: wild type	CGC	WB Strain: N2
C. elegans: NWG0076: *par-6(mib25[par-6::mCherry-LoxP]) I; par-2(it328[gfp::par-2]) III*	This paper	NWG0076
C. elegans: NWG0091: *pkc-3(it309 [gfp::pkc-3]) II; par-2(it315[mCherry::par-2]) III*	This paper	NWG0091
C. elegans: NWG0150: *nmy-2(cp52[nmy-2::mkate2 + LoxP unc-119(+) LoxP]) I; par-3(it298 [par-3::gfp]) III*	This paper	NWG0150
C. elegans: NWG0189: *par-3(cp54[mNG::3xFlag::par-3]) III*	Dan Dickinson	NWG0189
C. elegans: NWG0192: *par-2(crk30[par-2(R183-5A)::gfp]*it328) III*	This paper	NWG0192
C. elegans: NWG0240: *par-2(crk41[mNG::par-2 (C56S)]*cp329) / sC1(s2023) [dpy-1(s2170) umnIs21] III*	This paper	NWG0240
C. elegans: NWG0258: *par-6(mib25[par-6::mCherry-LoxP]) I; par-2(it328[gfp::par-2]) III; par-3(crk46[par-3(S950A)]) III*	This paper	NWG0258
C. elegans: NWG0259: *par-3(crk47[mNG::3xFlag::par-3 (S950A)]*cp54) III*	This paper	NWG0259
C. elegans: NWG0268: *par-6(cp45[par-6::mNeonGreen::3xFlag + LoxP unc-119(+) LoxP]) I; par-2(it315[mCherry::par-2]) III; unc-119(ed3) III*?	This paper	NWG0268
C. elegans: NWG0283: *nmy-2(ne3409) I; par-6(mib25[par-6::mCherry-LoxP]) I; par-2(it328[gfp::par-2]) III*	This paper	NWG0283
C. elegans: NWG0290: *par-6(mib25[par-6::mCherry-LoxP]) I; lgl-1(crk67[lgl-1::GFP]) X*	Rodrigues et al.[60]	NWG0290
C. elegans: NWG0316: *pkc-3(crk77[I331A,T394A]) II; par-2(it328[gfp::par-2]) III*	Ng et al.[27]	CGC Strain: NWG0316
C. elegans: NWG0319: *nmy-2(ne3409) I; par-6(mib25[par-6::mCherry-LoxP]) I; par-2(it328[gfp::par-2]) III; par-3(crk46[par-3(S950A)]) III*	This paper	NWG0319
C. elegans: NWG0332: *par-2(it315[mCherry::par-2]) III; par-1(ax4206) V*	This paper	NWG0332

(*Continued on next page*)

Continued

REAGENT or RESOURCE	SOURCE	IDENTIFIER
C. elegans: NWG0343: *par-6(mib25[par-6::mCherry-LoxP]) I; par-1(ax4206) V*	This paper	NWG0343
C. elegans: NWG0344: *par-2(crk3[par-2(S241A)::mCherry]*it315)/ sC1(s2023) [dpy-1(s2170) umnIs21] III; par-1(ax4206) V*	This paper	NWG0344
C. elegans: NWG0360: *par-6(mib25[par-6::mCherry-LoxP]) I; par-2(crk96[par-2(S241A)]) III; par-1(ax4206) V*	This paper	NWG0360
C. elegans: NWG0397: *par-2(it315[mCherry::par-2]) III; par-3(crk64[mNG::3xFlag::par-3(Δ69-82)]*cp54)/ qC1[dpy-19(e1259) glp-1(q339) qIs26] III*	This paper	NWG0397
C. elegans: NWG0453: *par-2(it315[mCherry::par-2]) III; par-3(cp54[mNG::3xFlag::par-3]) III*	This paper	NWG0453
C. elegans: NWG0458: *pkc-3(crk77 [I331A,T394A]) II; par-2(it315[mCherry::par-2]) III; par-3(cp54[mNG::3xFlag::par-3]) III*	This paper	NWG0458
C. elegans: NWG0473: *par-2(crk159[mNG::par-2(S241A, GCN4(LI-4mer))*crk104])/ sC1(s2023) [dpy-1(s2170) umnIs21] III*	Illukkumbura et al.[25]	NWG0473
C. elegans: NWG0524: *par-2(cp329[mNG::par-2]) III; mex-5(ax3050[mCherry::mex-5]) IV*	This paper	NWG0524
C. elegans: NWG0525: *par-2(crk41[mNG::par-2(C56S)]*cp329)/ sC1(s2023) [dpy-1(s2170) umnIs21] III; mex-5(ax3050[mCherry::mex-5]) IV*	This paper	NWG0525
C. elegans: NWG0526: *pkc-3(crk77 [I331A,T394A]) II; par-2(it315[mCherry::par-2]) III; par-3(crk64[mNG::3xFlag::par-3 (Δ69-82)]*cp54)/ qC1[dpy-19(e1259) glp-1(q339) qIs26] III*	This paper	NWG0526
C. elegans: OD58: *unc-119(ed3) III; ltIs38[pAA1; pie-1::GFP:: PH(PLC1delta1) + unc-119(+)]*	CGC	WB Strain: OD58
Oligonucleotides		
PAR-2(C56S) sgRNA #1: 5' – /AltR1/rGrC rUrGrA rUrCrA rCrArC rArGrU rGrGrA rCrArG rGrUrU rUrUrA rGrArG rCrUrA rUrGrC rU/AltR2/ – 3'	IDT DNA	N/A
PAR-2(C56S) sgRNA #2: 5' – /AltR1/rUrC rGrArA rArArG rCrUrG rArUrC rArCrA rCrArG rGrUrU rUrUrA rGrArG rCrUrA rUrGrC rU/AltR2/ – 3'	IDT DNA	N/A
PAR-2(C56S) FWD ODN genotyping primer: 5'–GATTGCCAACTCATCGCCAC–3'	IDT DNA	N/A
PAR-2(C56S) REV ODN genotyping primer: 5'–TCCGGCAAAATTGGGGTTTT–3'	IDT DNA	N/A
PAR-2(C56S) repair template (MfeI restriction site): 5'–TGCATCAACGACGTTCAACAGCCGGTTCGACGCGATTTG AGCTCGGAACTCTTAAGCCCCCTGTGTGATCAATTGTTCG ACAGGGTTAGAACATGGAAA–3'	IDT DNA	N/A
PAR-2(R183-5A) sgRNA #1: 5' – /AltR1/rCrA rGrUrG rGrGrC rGrArC rGrGrC rGrGrU rGrUrG rGrUrU rUrUrA rGrArG rCrUrA rUrGrC rU/AltR2/ – 3'	IDT DNA	N/A
PAR-2(R183-5A) sgRNA #2: 5' – /AltR1/rUrU rGrGrC rGrArC rArGrU rGrGrG rCrGrA rCrGrG rGrUrU rUrUrA rGrArG rCrUrA rUrGrC rU/AltR2/ – 3'	IDT DNA	N/A
PAR-2(R183-5A) FWD ODN genotyping primer: 5'–TCACCGAGCACATTTGACCA–3'	IDT DNA	N/A
PAR-2(R183-5A) REV ODN genotyping primer: 5'–AGCTATTCGGGGCGGAAAAA–3'	IDT DNA	N/A
PAR-2(R183-5A) repair template (NotI restriction site): 5'–TCCCATCAAAATCTTTATTTTTTCAGCCCAATCACCCCA CACGCGGCCGCTCCACTGTCGCCAAGTGCTCGTCCCG CCAAAAGTTCTCTGAAAATCCCGC–3'	IDT DNA	N/A

(*Continued on next page*)

Continued		
REAGENT or RESOURCE	SOURCE	IDENTIFIER
PAR-3(S950A) sgRNA #1: 5' – /AltR1/rArA rArCrC rGrArC rGrCrU rCrArC rArArG rCrUrA rGrUrU rUrUrA rGrArG rCrUrA rUrGrC rU/AltR2/ – 3'	IDT DNA	N/A
PAR-3(S950A) sgRNA #2: 5' – /AltR1/rGrG rArGrA rGrCrA rUrUrA rArCrC rGrArC rCrUrG rGrUrU rUrUrA rGrArG rCrUrA rUrGrC rU/AltR2/ – 3'	IDT DNA	N/A
PAR-3(S950A) FWD ODN genotyping primer: 5'–ACCAGCAACTCGTGGAACAT–3'	IDT DNA	N/A
PAR-3(S950A) REV ODN genotyping primer: 5'–AGGTGGAGCACGTTCAGATG–3'	IDT DNA	N/A
PAR-3(S950A) repair template (MspI restriction site): TTAAAAATATAAAAATTAACCCGGTTTCAGATATGCTAAACC GACGCTCACAAGCTATGGAAAGTATAAATCGGCCAGTG GAGAGCATTCTCCGTGGA	IDT DNA	N/A
Recombinant DNA		
Ahringer Feeding RNAi: *perm-1*	Source BioScience	WB Clone: sjj_T01H3.4
Ahringer Feeding RNAi: *ptr-2*	Source BioScience	WB Clone: sjj_C32E8.8
Feeding RNAi: *ctrl*	Rodriguez et al.[26]	N/A
Ahringer Feeding RNAi: *mex-5*	Source BioScience	WB Clone: sjj_W02A2.7
Software and algorithms		
MATLAB	Mathworks	R2019a; RRID:SCR_001622
PIVlab	http://pivlab.blogspot.com/ [61]	2.62.0.0
Fiji	https://imagej.net/software/fiji/ [62]	RRID:SCR_002285
Metamorph	Molecular Devices	RRID:SCR_002368
Trackpy	http://soft-matter.github.io/trackpy/v0.4.1/ [63]	0.4.1
Spectral Autofluorescence Image Correction By Regression (SAIBR)	https://github.com/goehringlab/saibr_fiji_plugin[60]	N/A
Python	https://www.python.org/	3.8.8; RRID:SCR_008394
Other		
Polybead Microspheres 20.00μm	Polysciences	18329-5
Polybead Microspheres 18.8μm	Polysciences	18329

RESOURCE AVAILABILITY

Lead contact

Further information and requests for resources and reagents should be directed to and will be fulfilled by the Lead Contact, Nathan W. Goehring (nate.goehring@crick.ac.uk).

Materials availability

All unique materials generated in this study will be made available by the lead contact without restriction.

Data and code availability

This paper does not report original code. Any additional information required to reanalyze the data reported in this paper is available from the lead contact upon request. All data reported in this paper will be shared by the lead contact upon request.

EXPERIMENTAL MODEL AND SUBJECT DETAILS

C. elegans – strains and culture conditions

C. elegans strains were maintained on OP50 bacterial lawns seeded on nematode growth media (NGM) at 20°C or 15°C (for experiments involving temperature sensitive mutants) under standard laboratory conditions.[64] Zygotes were obtained from hermaphrodites unless otherwise noted. Analysis of embryos precludes determination of animal sex.

C. elegans – transgenic animals

Mutation by CRISPR-Cas9 was performed based on the protocol published by Arribere et al.[65] Briefly, tracrRNA (IDT DNA, 0.5 μL at 100 μM) and crRNA(s) for the target (IDT DNA, 2.7 μL at 100μM) with duplex buffer (IDT DNA, 2.8μL) were annealed together (5 min, 95C) and then stored at room temperature until required. An injection mix containing Cas9 (IDT DNA, 0.5μL at 10mg/mL), annealed crRNA, tracrRNA, and the repair template (IDT Ultramer) was incubated at 37C for 15 min and centrifuged to remove debris (10 min, 13,000 rpm). Young gravid adults were injected along with either a *dpy-10* or *unc-58* co-CRISPR injection marker[65] and mutants identified by PCR and sequence verified.

Bacterial strains

OP50 bacteria and HT115(DE3) were obtained from CGC. Feeding by RNAi used HT115(DE3) bacteria strains carrying the indicated RNAi feeding plasmid.

METHOD DETAILS

C. elegans – RNAi

RNAi by feeding was performed according to previously described methods.[66] Briefly, HT115(DE3) bacterial feeding clones were inoculated from LB agar plates to LB liquid cultures and grown overnight at 37°C in the presence of 50 μg/mL ampicillin (until a fairly turbid culture is obtained). To induce high dsRNA expression, bacterial cultures were then treated with 1 mM IPTG before spotting 150μL of culture onto 60 mm NGM agar plates (supplemented with 10 μg/ml carbenicillin, 1 mM IPTG) and incubated for 24 hr at 20°C. L3/L4 larvae were then added to RNAi feeding plates and incubated for 24-32 hours at either 20°C or 25°C.

Imaging – dissection, drug treatment and mounting for microscopy

Embryos were obtained by dissecting adult worms in 8-10μL of egg buffer (118 mM NaCl, 48 mM KCl, 2 mM $CaCl_2$ 2 mM $MgCl_2$, 25 mM HEPES, pH 7.3), and mounted with 18.8 μm (cortex imaging) or 20 μm (midplane imaging) polystyrene beads (Polysciences, Inc.) between a slide and coverslip as in Rodriguez et al.,[26] and sealed using VALAP (1:1:1, vaseline:lanolin:paraffin wax).

For laser ablation mediated extrusion of ABa and ABp in 4-cell stage embryos, embryos were dissected in 8-10 μL of Shelton's Growth Medium[67] and mounted with 20 μm polystyrene beads (Polysciences, Inc.) between a slide and coverslip, and sealed using VALAP as above.

For acute drug treatment and washout experiments, embryos were first permeabilized using either *ptr-2* or *perm-1* fRNAi. Embryos were then dissected in 8-10μL of Shelton's Growth Medium (with or without drugs),[67] and mounted with 18.8 μm polystyrene beads between a large and small coverslip sealed on two parallel edges with VALAP as in Goehring et al.[68] Buffer exchange is achieved through capillary action by placing a drop of solution at one side of the sample and touching a piece of filter paper at the opposite side.

For drug treatments, the respective concentrations and relative timings for drug addition / washout for each experiment are as follows: For inhibiting PAR-2 polarization in *pkc-3*^{AS} P1 embryos, 20 μM of 1NA-PP1 (Calbiochem, 529579) was washed in before P0 cytokinesis completion. To depolymerize microtubules in P1, 10 μg/ml nocodazole was washed in before P0 cytokinesis completion. To block cortical flows acutely before cytokinesis, we washed in 0.5 μM Latrunculin A after NEBD. To reactivate PAR polarity in symmetrized 2-cell *pkc-3*^{AS} embryos, worms were dissected directly in 100 μM of 1NA-PP1, zygotes were then tracked and after cytokinesis onset, the drug was washed out.

For FLUCS, embryos were dissected in 5μL of M9 buffer and mounted in between a large and small coverslip with 20 μm polystyrene beads. The sample was then sealed with nail polish and attached to a sapphire microscope slide equipped with Peltier cooling elements using aluminum foil tape.[31]

Imaging – acute temperature upshift

Rapid temperature upshift for *nmy-2(ts)* alleles was achieved by first preheating one objective lens (100X) to 25.5°C and setting room temperature to 18.5°C. Following, embryos were dissected and mounted onto an objective lens without a temperature collar (~18.5°C), and zygotes were tracked and imaged through cytokinesis. 3 minutes after cytokinesis completion in P1 (and 5 minutes for P2), the objective lens was swapped with the preheated one (which roughly takes 30 to 60s), and imaging was continued. The 3 (or 5) minute buffer time was to ensure that cells do not re-fuse following cytokinesis as previously reported.[23] Disruption of *nmy-2(ts)* activity was confirmed by scoring cytokinesis failure following upshift. For FLUCS experiments, the sample was initially temperature controlled at 14.5°C using the Peltier stage, and was shifted to 26°C following FLUCS (roughly 6 minutes after cytokinesis).

Imaging – live imaging

Midsection confocal images were captured on a Nikon TiE with a 100x/1.40 NA oil objective, further equipped with a custom X-Light V1 spinning disk system (CrestOptics, Rome, Italy) with 50 μm slits, Obis 488/561 fiber-coupled diode lasers (Coherent, Santa Clara, CA) and an Evolve Delta EMCCD camera (Photometrics, Tucson, AZ). Imaging systems were run using Metamorph (Molecular Devices, San Jose, CA) and configured by Cairn Research (Kent, UK). Filter sets were from Chroma (Bellows Falls, VT): ZT488/561rpc, ZET405/488/561/640X, ET535/50m, ET630/75m. Imaging of cortical flows using NMY-2::GFP embryos was achieved as above, but by acquiring a stack instead with 5s intervals. The maximum intensity projection of the stack for each time point was then used for

further analysis.[69] All embryos were imaged with a 20ºC temperature collar, except for the temperature sensitive experiments, to which the temperature collar was set at 25.5ºC.

Cortical imaging was carried out with a 100x/1.49 NA TIRF objective on a Nikon TiE microscope equipped with an iLas2 TIRF unit (Roper), a custom-made field stop, 488 or 561 fiber coupled diode lasers (Obis), and an Evolve 512 Delta EMCCD camera (Photometrics), controlled by Metamorph software (Molecular Devices) and configured by Cairn Research. Filter sets were from Chroma: ZT488/561rpc, ZET488/561x, ZET488/561m, ET525/50m, ET630/75m, ET655LP. Images were captured in bright field, GFP/mNG (ex488/ZET488/561m), RFP/mKate/mCherry (ex561/ZET488/561m).

Confocal imaging for FLUCS was carried out using D_2O (Sigma-Aldrich) as the immersion fluid on an Olympus IX83 spinning disk system (GFP ex488, ET525/50m; mCherry ex561, ET617/73m) equipped with a 60x/1.2 NA water immersion objective (UPLSAPO, W-IR coating, Olympus), a Yokogawa W1 CSU scanner unit, and a Hamamatsu ORCA-Fusion Camera, and controlled using the cellSens Dimension software.

Imaging – laser ablation

To extrude ABa and ABp, we ablated a small circular region encompassing the anterior side of ABa and the eggshell, and the dorsal side of ABp and the eggshell with a 355nm laser using a iLas2 Pulse targeted illumination system (Roper). In successfully ablated embryos, cells lysed and extruded their contents out of the resulting perforation of the eggshell.

Imaging – FLUCS

Artificial hydrodynamic flows were generated by scanning an 1455 infrared laser at 1kHz around the cell edge of P1 cells using a polygon line path (Rapp OptoElectronic). Following cytokinesis of the zygote, we performed for FLUCS for roughly 5 mins, changing the line path as required due to slight changes in the shape of P1 during the FLUCS process. For the FLUCS control, an alternating bidirectional line scan path was used, changing directions between each scan to cancel out any induced flows.

QUANTIFICATION AND STATISTICAL ANALYSIS

Image analysis - particle image velocimetry

The mean flow velocity of NMY-2 was calculated via particle image velocimetry (PIV) using the PIVlab MATLAB plugin.[61] Briefly, maximum intensity projection of stacks was first processed using a rolling ball background subtraction and a 1 pixel median filter in Fiji. A box encompassing the entirety of P1 was selected as the ROI and was subjected to a high-pass filter with other preprocessing filters disabled. A FFT phase-space PIV algorithm was utilized with a 3 step multi pass linear window deformation, with a final area of 16 pixels. A velocity filter with a limit of 10 pixels per frame was applied together with a standard deviation filter, where any vectors that are 3 standard deviations from the mean are removed. Interpolation was used to replace lost vectors.

Image analysis – quantification of membrane profile

Raw or SAIBR processed images were used for quantification.[60] In order to measure cortical concentrations, a 100-pixel-wide (15.5 μm) line following the membrane around the embryo was computationally straightened, and a 20-pixel-wide (3.1 μm) rolling average filter was applied to the straightened image. Intensity profiles perpendicular to the membrane at each position were fit to the sum of a Gaussian component, representing membrane signal, and an error function component, representing cytoplasmic signal, and a constant, representing background signal. Membrane concentrations at each position were calculated as the amplitude of the Gaussian component. This protocol is similar to previously published methods[52,70] and identical to Ng et al.[27]

Image analysis – defining anterior and posterior poles in the zygote

The overall geometry of the zygote was first defined by fitting the shape of the ROI to an ellipsoid. The anterior and posterior poles were defined as the ROI coordinates nearest to the tip of each side of the major axis.

Image analysis – alignment of time series data in P1

Because PAR domains are more variable in position during polarization in P1, membrane profiles were aligned throughout the cell cycle for each embryo, followed by alignment between embryos to ensure accurate representation of PAR polarization dynamics. To align membrane concentration profiles throughout the cell cycle of an embryo, membrane profiles that were adjacent in time were averaged; individual profiles within that time span were aligned to the mean, and this process was iterated until a lowest mean squared error was obtained. To align membrane profiles between embryos, an averaged membrane profile for time points around NEBD was used as a reference for each embryo, and aligned in a manner identical to above, i.e. the membrane profiles of individual embryos were aligned to the mean of all embryos, and the process was iterated until the lowest mean squared error was achieved. Membrane profiles were also geometrically corrected via automated tracing of the ROIs in both clockwise and anti-clockwise fashion, and to invert membrane profiles of individual embryos so that the average of all embryos has the lowest mean squared error when aligned.

Image analysis – ASI

For calculating ASI, the following equation was used: ASI = (A – P) / (2 * (A + P)), where A and P denote the sum of fluorescence signals in the anterior or posterior 30% of the cell respectively.[26]

Image analysis – domain size

Normalized fluorescence profiles from pole to pole were fit to an error function as in prior work[26,27] according to the following:

$$I(x) = h * (1 + erf((x - c) / \sigma))$$

where erf is the error function, c is the center of the domain boundary position, σ is the spread of the boundary, and h allows for scaling of domain intensity. Domain size is then defined as a fraction of the total pole to pole length, L:

$$(L - (c - 0.75\sigma)) / L.$$

Image analysis – particle detection and tracking

Single molecule and cluster tracking were carried out in Python using the Trackpy package (https://github.com/soft-matter/trackpy). It implements the Crocker-Grier algorithm to localize particles to subpixel resolution in individual frames by fitting local intensity peaks to a Gaussian point spread function. Detection parameters such as the threshold intensity and diameter of the candidate particles were adjusted empirically for given imaging conditions. Particles were linked frame to frame, with additional user-specified parameters. Parameters were optimized to minimize tracking errors and typically were as follows: feature size = 5 pixels, memory = 0 frames, minimum separation between features = 7 pixels, maximum distance features can move between frames = 6 pixels, minimum track length = 10 frames.

Statistics

All statistical tests were performed in Python and indicated in the figure legends. Data points are shown along with mean values ± 95% confidence interval (bootstrapped) unless otherwise noted. Reported N are the number of embryos analyzed.